Charge transport mechanisms in inkjet-printed thin-film transistors based on two-dimensional materials

Charge transport mechanisms in inkjet-printed thin-film transistors based on two-dimensional materials

Erik Piatti,[1,*] Adrees Arbab,[2,3,*] Francesco Galanti,[1] Tian Carey,[3] Luca Anzi,[4] Dahnan Spurling,[5] Ahin Roy,[5] Ainur Zhussupbekova,[5] Kishan A. Patel,[4] Jong M. Kim,[6] Dario Daghero,[1] Roman Sordan,[4] Valeria Nicolosi,[5] Renato S. Gonnelli,[1] and Felice Torrisi[3,†]

[1] *Department of Applied Science and Technology, Politecnico di Torino, I-10129 Torino, Italy*
[2] *Cambridge Graphene Centre, University of Cambridge, Cambridge CB3 0FA, UK*
[3] *Department of Chemistry, Molecular Sciences Research Hub, Imperial College London, White City Campus, Wood Lane, London, W12 0BZ, UK*
[4] *L-NESS, Department of Physics, Politecnico di Milano, I-22100 Como, Italy*
[5] *Trinity College Dublin, Dublin 2, Ireland*
[6] *Department of Engineering, University of Cambridge, Cambridge CB3 0FA, UK*

Printed electronics has emerged as a pathway for large scale, flexible, and wearable devices enabled by graphene and two-dimensional materials. However, the complexity of the ink formulations, and the polycrystalline nature of the resulting thin films, have made it difficult to examine charge transport in such devices so far. Here we identify and describe the charge transport mechanisms of surfactant- and solvent-free inkjet-printed thin-film devices of representative few-layer graphene (semi-metal), molybdenum disulfide (MoS_2, semiconductor) and titanium carbide MXene (Ti_3C_2, metal) by investigating the temperature, gate and magnetic field dependencies of their electrical conductivity. We find that charge transport in printed few-layer MXene and MoS_2 devices is dominated by the intrinsic transport mechanism of the constituent flakes: MXene exhibits a weakly-localized 2D metallic behaviour at any temperature, whereas MoS_2 behaves as an insulator with a crossover from 3D-Mott variable-range hopping to nearest-neighbour hopping around 200 K. Charge transport in printed few-layer graphene devices is dominated by the transport mechanism between different flakes, which exhibit 3D-Mott variable range hopping conduction at any temperature. These findings pave the way for a reliable design of printed electronics with two-dimensional materials.

Cite this article as:
Piatti, E., Arbab, A., Galanti, F. *et al.*. Charge transport mechanisms in inkjet-printed thin-film transistors based on two-dimensional materials. *Nat. Electron.* **4,** 893–905 (2021).

DOI:
10.1038/s41928-021-00684-9

Printable inks based on graphene and other two-dimensional (2D) materials could be used to make high-performance flexible [1–6] and wearable electronics [1, 7, 8]. Electronic inks from 2D materials (E2D inks) are mixtures of a functional 2D material, stabilizers, and rheology modifiers. E2D inks with different electronic properties have been developed to print the different elements of a device: semiconducting or semimetallic inks in the active layer, insulating inks for dielectrics, and conducting inks for electrodes.

Large-scale production of E2D inks [2, 3] has been reported using solution-processing techniques such as electrochemical exfoliation [9, 10] and liquid-phase exfoliation (LPE), including shear mixing [11], microfluidization [3, 6] and ultrasonication [12–14]. Several printing methods such as inkjet printing [3, 4, 15], screen printing [6, 16], flexographic printing [17], and spray coating [18, 19] have been used to demonstrate electronic [1, 20], optoelectronic [21, 22], and photonic [23, 24] devices. Drop-on-demand (DoD) inkjet printing is a particularly promising approach because it works with a wide range of substrates (e.g. textile, polymers and silicon) in a maskless and non-contact deposition mode, and offers high resolution ($\sim 50\,\mu m$) and low material losses (< 1 ml) [25].

Inkjet-printed field-effect transistors (FETs) with graphene inks have demonstrated mobilities of up to $\sim 204\,cm^2V^{-1}s^{-1}$ on Polyethylene terephthalate (PET) substrates [3], while current modulation in printed E2D inks has also been achieved using ionic gating with a spray-coated hexagonal boron nitride as a porous separator [4]. Inkjet-printed E2D ink photodetectors [5, 26] achieved photoresponsivities of up to $\sim 50\,mA\,W^{-1}$, using MoS_2 on Polyimide (PI) [26]. As a result, there is now a substantial industrial interest in using E2D inks for applications in printed wearable electronics and electronic-textiles (e-textiles) [1], currently incompatible with organic or inorganic semiconductors. A technology roadmap for electronics based on E2D inks urges a thorough understanding of the charge transport mechanisms in printed thin films of E2Ds, enabling an accurate description of the physics in such devices [27, 28].

However, though charge transport mechanisms in isolated flakes of 2D materials – including MoS_2 [29–32], graphene [33–35] and MXenes [36, 37] – have been exten-

* These authors contributed equally.
† Corresponding author: f.torrisi@imperial.ac.uk

sively investigated, the mechanism in inkjet-printed films of E2D inks remains poorly understood. This is because the structure of inkjet-printed films consists of a large number of highly-crystalline flakes assembled together in a three-dimensional network [1], and is more complex than that of isolated flakes. As a result, transport in these structures depends on an interplay between charge-carrier propagation within each flake (*intra*-flake transport) and propagation from one flake to the surrounding flakes in the network (*inter*-flake transport) [38]. This makes inkjet-printed films of E2D inks a prime example of granular conductors with 2D material units, and inevitably introduces additional disorder with respect to that found in isolated flakes in the form of the sharp boundaries between the different printed flakes in the network [2].

In this context, gate-, temperature-, and magnetic field-dependent conductivity measurements are powerful tools to investigate charge transport in disordered materials (see Methods). An early attempt to probe low-temperature conductivity in printed thin films of semiconducting transition metal dichalcogenides suggested that charge transport occurred via some kind of hopping mechanism, but failed to reach a conclusion on the specific model [4]. In this work, we determine the transport mechanisms in metallic, semimetallic and semiconducting inkjet-printed E2D-ink films by examining the temperature, gate and magnetic field dependencies of their electrical conductivity. Our inkjet-printed field-effect devices are made from surfactant-free titanium carbide (Ti_3C_2) MXene, graphene and MoS_2 inks and are composed of a network of 2D material flakes. We demonstrate that in the printed MXene and MoS_2 devices, the charge transport is dominated by *intra*-flake processes and mirrors that in the isolated constituent flakes. In the printed graphene devices the transport is dominated by *inter*-flake processes and deviates from the semimetallic behaviour of isolated graphene.

INK FORMULATION AND MATERIAL CHARACTERISATION

Typically E2D ink formulations require the use of additives such as binders (substances which cohesively hold materials together) or surfactants, which degrade the electrical properties of the ink [2, 3, 27] as most of the binders and surfactants hinder the hopping of charge carriers through a film of 2D materials. Solvent-exchange techniques have been successfully adopted on exfoliated layered material dispersions to produce stabiliser-free low boiling point ($< 100\,^{\circ}C$) E2D inks in ethanol, for inkjet-printed electronics [3]. Here we adopt a solvent-exchange technique (see Methods) yielding pure graphene, MoS_2 and Ti_3C_2 low-boiling-point inks in ethanol suitable for inkjet-printing. The graphene ink was prepared by ultrasonic exfoliation of graphite (see Methods) following our previous work. [3] The MXene ink was produced by etching the aluminium in MAX powder using the in-situ hydrofluoric acid method (see Methods) [20], while the MoS_2 ink was prepared by electrochemical exfoliation of bulk MoS_2 layered crystals via quaternary ammonium molecules (see Methods) [10]. We measure the optical absorption spectra in the ultraviolet-visible (UV-Vis) range to estimate the flake concentration, c, via the Beer-Lambert law (see Methods) for the MXene (Fig. 1a), graphene (Fig. 1b) and MoS_2 (Fig. 1c) inks, respectively. We obtain $c_{MX} \sim 0.50\,mg\,ml^{-1}$, $c_{GR} \sim 0.495\,mg\,ml^{-1}$ and $c_{MS} \sim 2.73\,mg\,ml^{-1}$ for the MXene, graphene and MoS_2 inks. The UV-Vis spectrum of the graphene ink is mostly featureless as expected [39], with a prominent peak at $\sim 268\,nm$ which can be attributed to the Van Hove singularity in the graphene density of states (DOS) [39]. The UV-Vis spectrum of the MoS_2 ink shows the characteristic A ($\sim 610\,nm$) and B ($\sim 675\,nm$) excitonic peaks of the $2H$ semiconducting crystal phase [40], as well as a broader feature at $\sim 420\,nm$ due to the convolution of the C and D excitonic peaks [41]. The UV-Vis spectrum of the MXene ink shows a distinct peak at $\sim 260\,nm$ which originates from surface termination groups (-F, -OH and -O) [42, 43] during the etching process (see Methods) [44]. The MXene ink also has a broad peak at $\sim 800\,nm$ which is associated to a transversal surface plasmon in the MXene flakes [45–47], which is greatly enhanced upon functionalisation of their surface with aluminium (Al) oxoanion groups [48]. We employ energy-dispersive X-ray spectroscopy (EDX) to confirm the removal of Al from the MAX phase precursor during the etching process to form the MXene ink (see Fig. S1). The EDX Al signal at $\sim 1\,keV$ is substantially weak compared to that of titanium (Ti) and carbon (C), and comparable to the signal obtained for high-quality Ti_3C_2 MXenes in previous reports [42–44]. We then validate the suitability of the inks for inkjet printing using these parameters to calculate the figure of merit Z (see Methods) [49], finding $Z_{GR} \sim 22$, $Z_{MS} \sim 11$ and $Z_{MX} \sim 4$ for graphene, MoS_2 and MXene inks respectively, in accordance with previous reports on inkjet-printed E2D inks [3, 15].

Atomic force microscopy (AFM) is used to estimate the lateral size $\langle S \rangle$ and average thickness t_{av} of the 2D-material flakes (see Methods and Figs. S2-S4). Figs. 1d-f show the statistical distributions of $\langle S \rangle$ and t_{av} in the form of a histogram for MXene, graphene and MoS_2 inks. A log-normal distribution peaked at $\langle S \rangle_{MX} \sim 710\,nm$, $\langle S \rangle_{GR} \sim 208\,nm$ and $\langle S \rangle_{MS} \sim 478\,nm$ appears for the MXene, graphene and MoS_2 flakes, respectively. This confirms that the flake dimensions fall within the required range for DoD inkjet printing [15]. We also find the average flake thickness for the MXene, graphene and MoS_2 inks to be $t_{av,MX} \sim 3.5\,nm$, $t_{av,GR} \sim 6.5\,nm$ and $t_{av,MS} \sim 1.7\,nm$. Transmission electron microscopy (TEM) corroborates the distribution of the lateral size of the flakes in the inks (Figs. 1g-i), showing that the MXene inks can have flakes with $\langle S \rangle \geq 1\ \mu m$, whereas the graphene and MoS_2 flakes tend to be in the range of

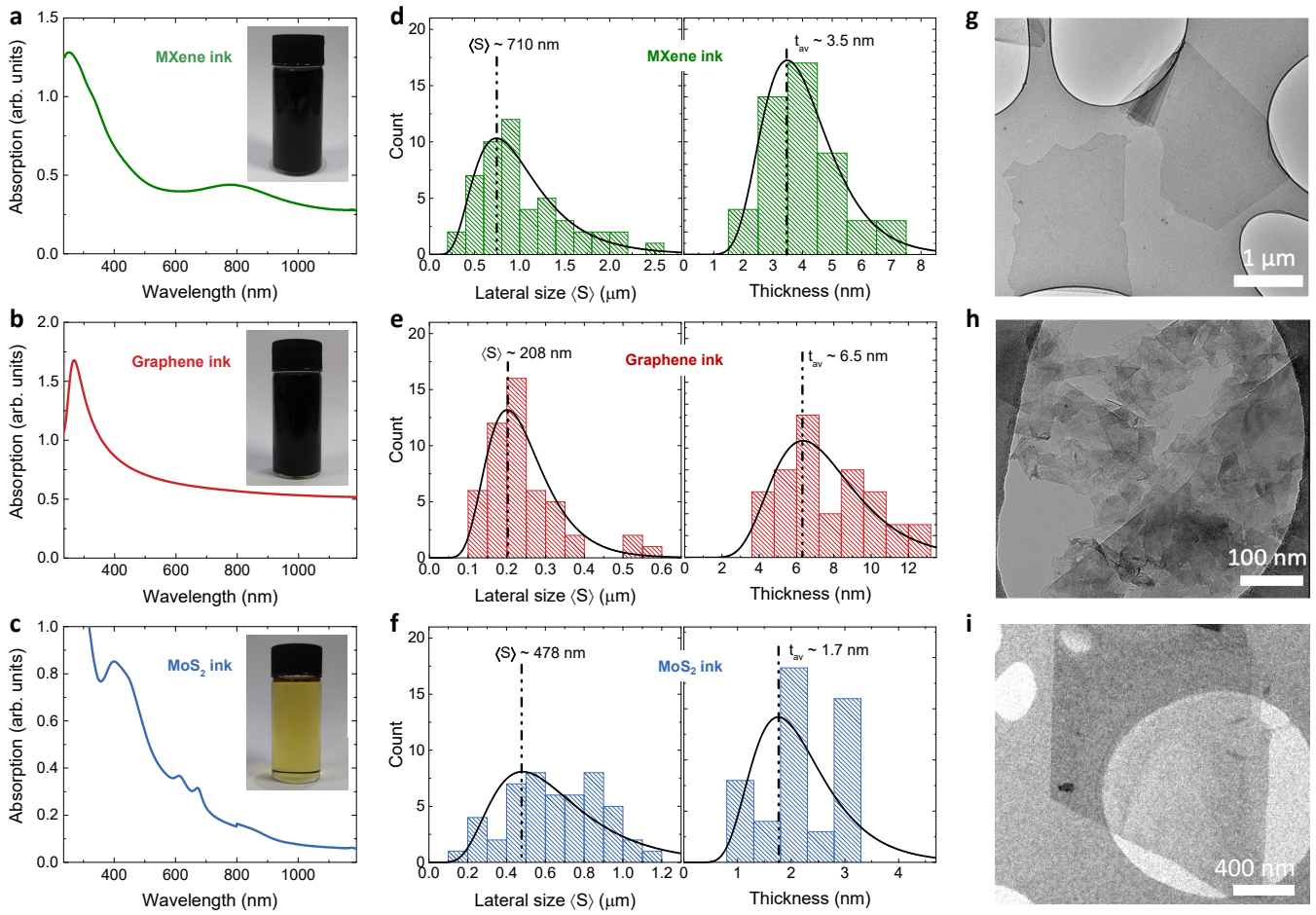

FIG. 1. UV-Vis, AFM and TEM of the E2D inks. Ultraviolet spectroscopy of **a** the MXene, **b** the graphene, and **c** the MoS_2 inks used to make thin films. Insets show the photographs of the corresponding solvent-dispersed 2D material flakes. Statistics of the lateral size and thickness of **d** the MXene, **e** the graphene, and **f** the MoS_2 flakes in the E2D inks. Transmission electron microscope image of **g** the MXene, **h** the graphene, and **i** the MoS_2 flakes in the E2D inks.

$\langle S \rangle \sim 200 - 900\,\text{nm}$.

We then employ Raman spectroscopy to examine the structural quality of the E2D flakes and X-ray photoelectron spectroscopy to assess their stoichiometry (see Methods). In the MXene ink, the Raman spectrum (Fig. 2a) shows two broad resonant regions, typical of Ti_3C_2 MXene (see Supplementary Section V), denoted as the T_x region betweeen $\sim 223\,\text{cm}^{-1}$ and $\sim 480\,\text{cm}^{-1}$, and the C region between $\sim 503\,\text{cm}^{-1}$ and $750\ \text{cm}^{-1}$. An additional peak appears at $\sim 205\,\text{cm}^{-1}$ and is caused by an A_{1g} out-of-plane vibrational mode that originates from the C atoms, the two Ti layers and the functional -OH, -O and -F surface groups [50]. This is confirmed by the EDX spectra (see Methods) showing the presence of -O, -F and minor traces of -Cl (see Fig. S1).

Fig. 2b shows the XPS spectrum of the C 1s and Ti 2p regions for the MXene ink, that confirms the formation of Ti_3C_2 from the MAX phase powder. The C 1s region comprises six non-doublet peaks belonging to graphitic C-C formation, Ti carbide and Ti-C bonds, C-OH and C-O-C bonds, and C-H functional group on the surface of the MXene flakes (see Supplementary Section VI). The Ti 2p region contains three doublet peaks associated with the $Ti_3C_2O_x$ and $Ti_3C_2(HO)$ functional groups on the MXene flake surface [50, 51]. The asymmetric Ti-C ($2p_{3/2} \sim 454.8\,\text{eV}$ and $2p_{1/2} \sim 460\,\text{eV}$) peak which is commonly associated with MXene flakes is shifted to a larger binding energy compared to its precursor MAX phase powder. This is attributed to the Al in the MAX phase powder (Ti-C $2p_{3/2} \sim 454.6\,\text{eV}$) being replaced by a more electronegative termination group like -F, -O, and -OH [51–54].

The Raman spectrum of the graphene ink (Fig. 2c) shows the characteristic G and D peaks at $\sim 1581\,\text{cm}^{-1}$ and $\sim 1349\,\text{cm}^{-1}$, a D+D′ peak at $\sim 2950\,\text{cm}^{-1}$ and a Lorentzian-shaped 2D peak positioned at $\sim 2700\,\text{cm}^{-1}$. These indicate the graphene film comprises of electronically-decoupled graphene layers (see Methods). In pristine graphene inks, the D peak corresponds to the flake edges, rather than to the presence of a disorder

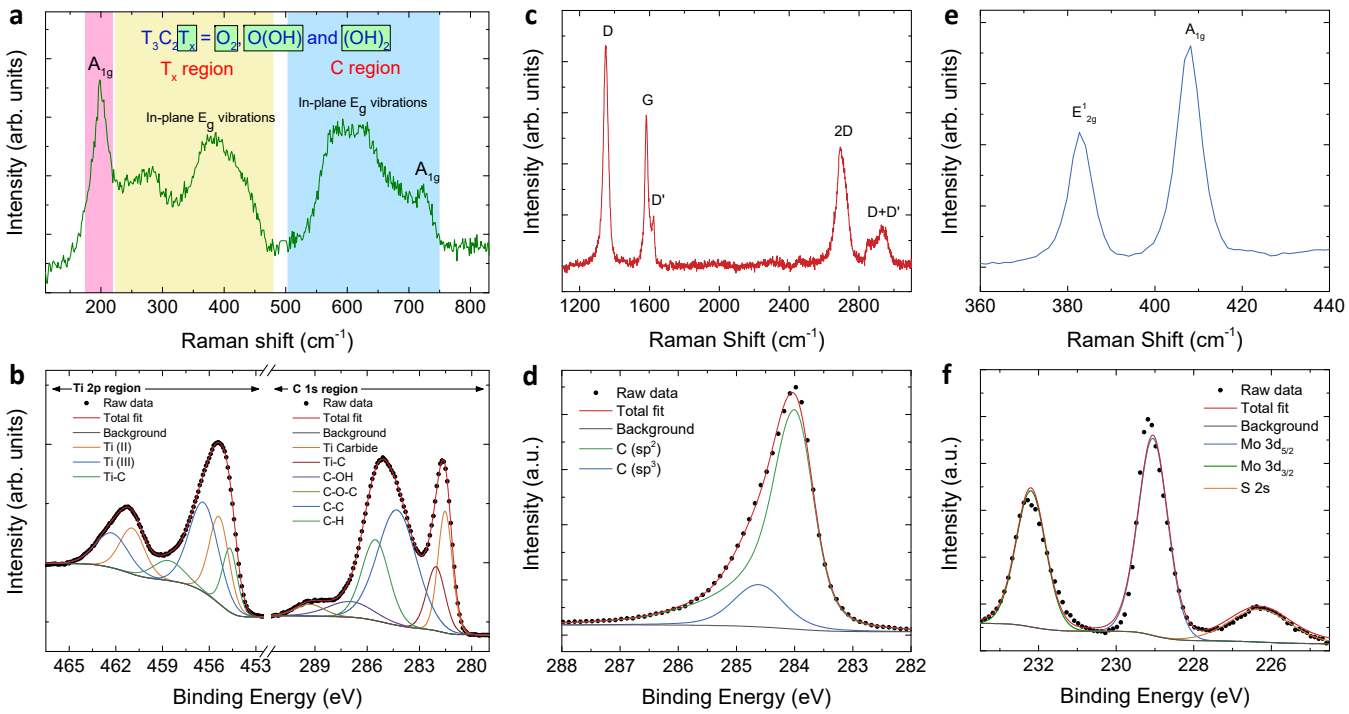

FIG. 2. Raman and XPS spectroscopies of the E2D inks. **a** Raman spectrum of the MXene ink. Blue and pink shaded areas indicate the in-plane and the out-of-plane modes, due either to termination groups (T_x region) or to C atoms (C region). **b** XPS of the MXene ink, showing the C 1s and the Ti 2p regions. **c** Raman spectrum of the graphene ink and **d** its XPS, showing the C region comprising sp^2 and sp^3 C atoms. **e** Raman spectra of the MoS_2 ink **f** and its XPS showing the Mo region. All Raman spectra were acquired at 514.5 nm.

within the flakes [15, 55]. The D+D′ peak is attributed to a two-photon defect-assisted process [55]. The XPS spectrum of the graphene ink (Fig. 2d) shows a convoluted peak, composed of two peaks associated with the sp^2 and sp^3 carbon atoms [56]. The sp^2 peak (green curve) at ~ 283.9 eV has a broad and asymmetric tail at higher binding energies, which is not present in the case of the sp^3 peak (blue curve) at ~ 284.7 eV. Integrating the area under the two curves reveals a ratio of 80%:20% (sp^2:sp^3), which implies that the majority of C atoms are sp^2 hybridised (see Methods).

In the MoS_2 ink, the Raman spectrum (Fig. 2e) shows the typical E^1_{2g} and A_{1g} peaks that appear at ~ 382.5 and $\sim 407\,cm^{-1}$, respectively. The position of both peaks indicates a high crystallinity of the flakes [57]. Fig. 2f shows the XPS spectrum of the MoS_2 inks, which exhibits the $3d_{3/2}$ and $3d_{5/2}$ doublet peaks associated with molybdenum (Mo) that appear at ~ 232 eV and ~ 229 eV, respectively. The XPS spectrum also shows a 2s peak originating from the sulfur (S) atoms in MoS_2 [58].

INKJET-PRINTED 2D MATERIAL THIN-FILM DEVICES

We fabricate the graphene and MXene thin-film devices by inkjet printing the graphene and MXene inks on p-doped Si/SiO_2 substrates, and the MoS_2 thin-film devices by inkjet printing the MoS_2 ink on a pre-patterned substrate (see Methods). We additionally fabricate flexible graphene films on PET as detailed in Ref. 3 for comparison. The low boiling point of our E2D inks improves the morphological uniformity and assists in the solvent removal after printing [18]. When inkjet printing, the ejected drop contacts the substrate as discussed in Supplementary Section VII (Figs. S5 and S6), followed by annealing (see Methods). AFM and profilometer data show that the rectangular printed films of graphene, MXene, and MoS_2 inks have thickness respectively of $t_{d,GR} \sim 130$ nm, $t_{d,MX} \sim 30$ nm and $t_{d,MS} \sim 40$ nm (Figs. S2, S3 and S4), which were selected to ensure that the percolation threshold for each E2D ink is achieved [59].

The inkjet-printed thin-film devices were then contacted for charge transport measurements (see Methods), as shown schematically in Figs. 3a,b for graphene/MXene and MoS_2 devices, respectively. Fig. 3c plots the conductivity σ as a function of temperature T for the inkjet-printed MXene, graphene and MoS_2 thin-film devices at

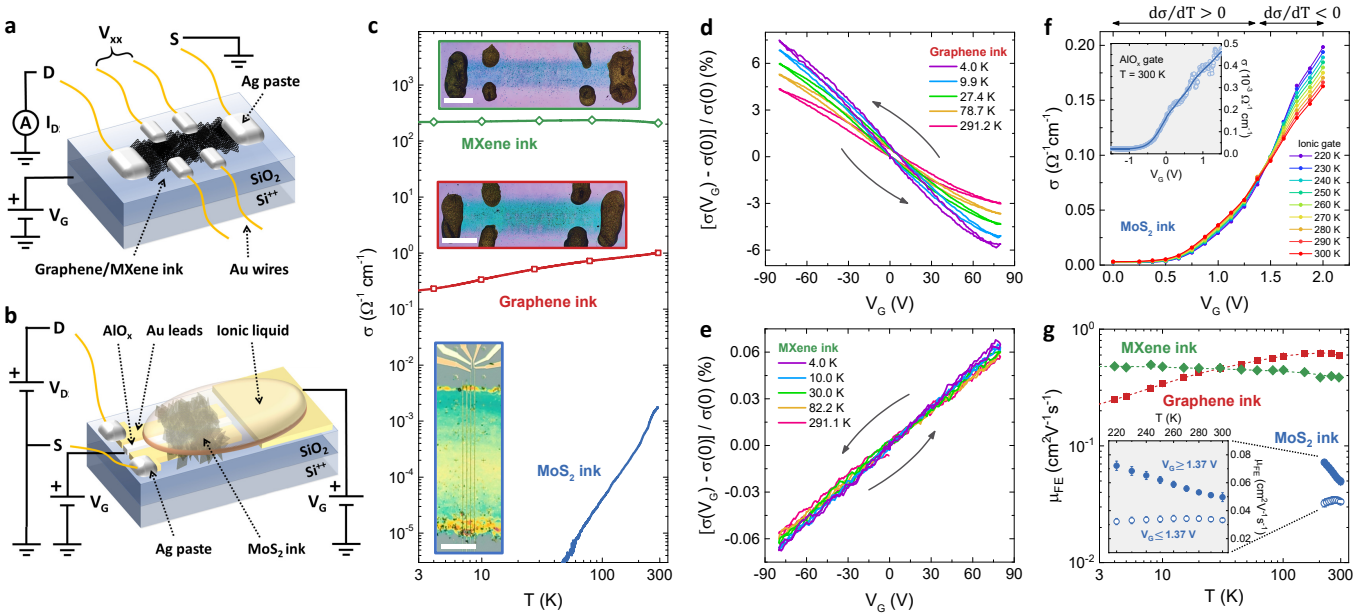

FIG. 3. Charge transport measurements in E2D-ink transistors. Sketch of: **a**, an inkjet-printed graphene/MXene field-effect device, and **b**, an inkjet-printed MoS_2 device. **c**, Conductivity σ at gate voltage $V_G = 0$ as a function of temperature T in E2D-ink FETs, in double logarithmic scale. Solid blue, red and green lines are the σ of a printed MoS_2-ink device, a printed graphene-ink device, and a printed MXene-ink device respectively. Hollow symbols are the values of $\sigma(0)$ for which the V_G sweeps are shown in panels **d**,**e**. Insets show the optical images of a printed MXene device (green border, scale bar 4 mm), a printed graphene device (red border, scale bar 4 mm) and a printed MoS_2 device (blue border, scale bar 100 µm). **d**,**e**, Conductivity ratio $[\sigma(V_G) - \sigma(0)]/\sigma(0)$ as a function of V_G for increasing T in a printed graphene device (**d**) and in a printed MXene device (**e**). Black arrows indicate the direction of the V_G sweeps. **f**, σ of a printed MoS_2 device as a function of V_G applied to the ionic gate at different temperatures, constructed by starting from the curves of σ as a function of T at different V_G shown in Fig. 4c. Inset shows σ as a function V_G applied through the AlO_x via the Al gate electrode. **g**, Field-effect mobility μ_{FE} as a function of T in logarithmic scale for a printed graphene device (red squares), a printed MXene device (green diamonds) and a printed MoS_2 device (hollow blue circles, $V_G \leq 1.37$ V; filled blue circles, $V_G \geq 1.37$ V). Dashed lines are guides to the eye. The inset shows a magnification of the MoS_2 mobility in linear scale.

a gate voltage $V_G = 0$ (green, red and blue curves respectively; see Methods). At $T = 290$ K, the conductivity of the inkjet-printed devices spans over five orders of magnitude, ranging from $\sigma_{MS} = 1.7 \cdot 10^{-3}\,\Omega^{-1}\text{cm}^{-1}$ in the MoS_2-ink device, to $\sigma_{GR} = 1.1\,\Omega^{-1}\text{cm}^{-1}$ in the graphene-ink device, to $\sigma_{MX} = 208\,\Omega^{-1}\text{cm}^{-1}$ in the MXene-ink device. Between $T \sim 290$ K and ~ 50 K, σ_{MS} decreases by three orders of magnitude, consistent with the behaviour of ungated MoS_2 flakes [29–32], and falls below $3 \cdot 10^{-6}\,\Omega^{-1}\text{cm}^{-1}$ for $T \leq 50$ K. In the same T range, σ_{GR} also decreases with decreasing T, albeit only by a factor ~ 5 between $T \sim 290$ K and 5 K. These dependencies suggest that charge transport in both MoS_2-ink and graphene-ink devices occurs via hopping processes [60–62]. Inter-flake hopping is dominant in the graphene ink, since single flakes typically display a metallic-like behaviour [33–35], which is at odds with that observed in our films. In the MoS_2 ink the single flakes display an insulating-like behaviour, hence a deeper analysis is needed to understand whether *inter*- or *intra*-flake hopping mechanisms dominate. Conversely, σ_{MX} appears to be nearly T-independent in the scale of Fig. 3c, in line with reports on MXene epitaxial films [63], indicating that charge transport in MXene-ink devices should thus occur over extended states [60–62].

Fig. 3d,e shows the V_G-dependent conductivity ratio $[\sigma(V_G) - \sigma(0)]/\sigma(0)$ for a subset of T values for the graphene and MXene devices (see Fig. S7 for the full set of σ vs V_G curves), $\sigma(0)$ being shown in Fig. 3c as hollow symbols. Here σ_{GR} (Fig. 3d) decreases monotonically with increasing V_G, indicating intrinsic hole conduction induced by unintentional doping of adsorbed molecules [64]. A finite hysteresis suggests charge transfer with traps close to the graphene-SiO_2 interface [64]. Both features are typical of inkjet-printed graphene transistors [3, 15]. The maximum gate-induced modulation of σ_{GR} increases as T decreases, going from 7.5% at $T \sim 290$ K to 13.5% at $T \sim 4$ K, remaining smaller but in line with reported modulations in inkjet-printed graphene FETs [3, 15, 65]. σ_{MX} (Fig. 3e) increases monotonically with increasing V_G, indicating intrinsic electron conduction, without any hysteresis. Both findings are in agreement with the FET behaviour of single-layer MXene flakes [36, 37]. The maximum gate-induced mod-

ulation of σ_{MX} slightly increases as T decreases, going from $\sim$ 0.11% at $T \sim 290\,K$ to $\sim$ 0.14% at $T \sim 4\,K$, about two orders of magnitude smaller than that of the graphene devices and consistent with metallic behaviour. The modulation is also small compared to those of $\sim 1\%$ reported in single-layer MXene FETs [36, 37] due to the much larger thickness of our printed films. In the printed MoS_2 devices we first measured σ as a function of V_G applied through the Al/AlO_x gate stack at $T \sim 300\,K$ (see inset to Fig. 3f). σ_{MS} increases monotonically with V_G, indicating n-type behaviour, an on-off ratio of ~ 25, and a mobility of up to $\sim 10^{-1}\,cm^2V^{-1}s^{-1}$, in line with our recent results [66]. Below $T \sim 300\,K$ the response of σ_{MS} to the dielectric gating proved weak and we consequently switched to the ionic gate (see Methods). At $T \sim 300\,K$ the ionic-gate induced modulation of σ_{MS} exhibits n-type behaviour with an on-off ratio of ~ 50 (Fig. 3f), twice the one induced by the solid-oxide gate, and which increases to ~ 85 as T is lowered to 220 K. For $V_G \leq 1.37\,V$, σ_{MS} increases upon increasing T, similar to the ungated case shown in Fig. 3c, whereas an opposite dependence of σ_{MS} occurs for $V_G \geq 1.37\,V$. Above 220 K, this suggests the occurrence, of a gate-induced crossover from a hopping transport over localized states to a band-like transport over extended states.

Fig. 3g shows the field-effect mobility (see Methods) as a function of T for the MoS_2 device ($\mu_{FE,MS}$, blue circles), the graphene device ($\mu_{FE,GR}$, red squares) and the printed MXene device ($\mu_{FE,MX}$, green diamonds). $\mu_{FE,GR}$ decreases from ~ 0.6 to $\sim 0.2\,cm^2V^{-1}s^{-1}$ when the device is cooled from $T \sim 290\,K$ to $\sim 4\,K$, whereas $\mu_{FE,MX}$ slightly increases from ~ 0.4 to $\sim 0.5\,cm^2V^{-1}s^{-1}$ in the same T range, consistent with Hall effect measurements at low T (Fig. S8). The values of $\mu_{FE,MX}$ are in good agreement with those reported both in single-layer MXene FETs ($0.6 - 2.6\,cm^2V^{-1}s^{-1}$) [36, 37] and in thicker MXene films ($0.9 - 1\,cm^2V^{-1}s^{-1}$) [45, 67]. The weak increase of $\mu_{FE,MX}$ as T decreases is typical of disordered metallic systems where the main source of charge-carrier scattering comes from defects [60, 61]. The values of $\mu_{FE,GR}$ are instead lower than those reported for inkjet-printed graphene FETs on PET [3], possibly due to the more regular flake arrangement in the graphene films printed on PET substrate [3] with respect to films printed on SiO_2. This correlation with the morphology of the system is consistent with the conduction in the graphene films being dominated by inter-flake resistance. The monotonic increase of $\mu_{FE,GR}$ with increasing T below 200 K is expected when charge transport occurs via hopping processes [29, 68], whereas the saturation and slight decrease of $\mu_{FE,GR}$ between $T \sim 200\,K$ and 290 K suggest a non-negligible impact of electron-phonon (e-ph) scattering in this higher T range [29, 33, 34]. The values of $\mu_{FE,MS}$ are determined separately in the hopping (hollow circles) and band-like (filled circles) conduction regions above and below $V_G \sim 1.37\,V$ (see Methods): $\mu_{FE,MS}$ slightly decreases from ~ 0.034 to $\sim 0.032\,cm^2V^{-1}s^{-1}$ for $V_G \leq 1.37\,V$, and $\mu_{FE,MS}$ increases from ~ 0.049 to $\sim 0.072\,cm^2V^{-1}s^{-1}$, for $V_G \geq 1.37\,V$. These values are in agreement with those determined in the same devices in the absence of the ionic liquid (up to $\sim 10^{-1}\,cm^2V^{-1}s^{-1}$), and with those recently reported for inkjet-printed MoS_2 FETs [66] and ion-gated MoS_2 networks ($10^{-2} - 0.1\,cm^2V^{-1}s^{-1}$) [4, 69]. The opposite T-dependencies exhibited above and below $V_G \sim 1.37\,V$ again suggest a crossover from hopping transport at low V_G to a band-like one at high V_G, similar to the behaviour reported in disordered isolated MoS_2 flakes [29].

CHARGE TRANSPORT MECHANISMS

The charge transport mechanisms in our inkjet-printed E2D-ink devices can be determined by making use of robust models originally developed for disordered crystalline materials [60, 61], and lately validated for various granular systems [62] including 2D material networks [65, 69–72]. These describe charge transport in two distinct regimes, insulating (hopping transport) and metallic (transport over extended states), separated by the insulator-to-metal transition (IMT) [60, 61] governed by the ratio of the intra- and inter-flake conductances [62] (see Supplementary Section X). Note that structural parameters like flake size and thickness, degree of overlap and flake orientation, are expected to be of primary importance in the description of granular systems, mainly affecting the absolute value of the conductivity, rather than its temperature dependence, on which our analysis will be focused.

HOPPING TRANSPORT IN INKJET-PRINTED MOS_2 DEVICES

The electrical conductivity in any hopping regime follows a temperature dependence of the type [60–62]:

$$\sigma(T) = \sigma_0 \exp\left[-\left(\frac{T_0}{T}\right)^p\right] \quad (1)$$

where T_0 is a characteristic temperature, σ_0 is the conductivity for $T \to \infty$ and p is an exponent which depends on the specific type of hopping mechanism. In the nearest-neighbour hopping (NNH) mechanism, $p = 1$ and σ follows an activated behaviour with an activation energy $E_a = k_B T_0$ [60, 61], k_B being the Boltzmann constant. All variable-range hopping (VRH) mechanisms instead exhibit $p < 1$, with the Efros-Shklovskii VRH mechanism (ES-VRH) being characterised by $p = 1/2$ (meaning that a soft gap is opened in the DOS at the Fermi level [60–62]) and the Mott VRH mechanism exhibiting $p = 1/(1 + d)$, where d is the dimensionality of the system [60–62].

Fig. 4a shows σ_{MS} as a function of $T^{-1/4}$ in a representative MoS_2 device in the absence of V_G (ungated):

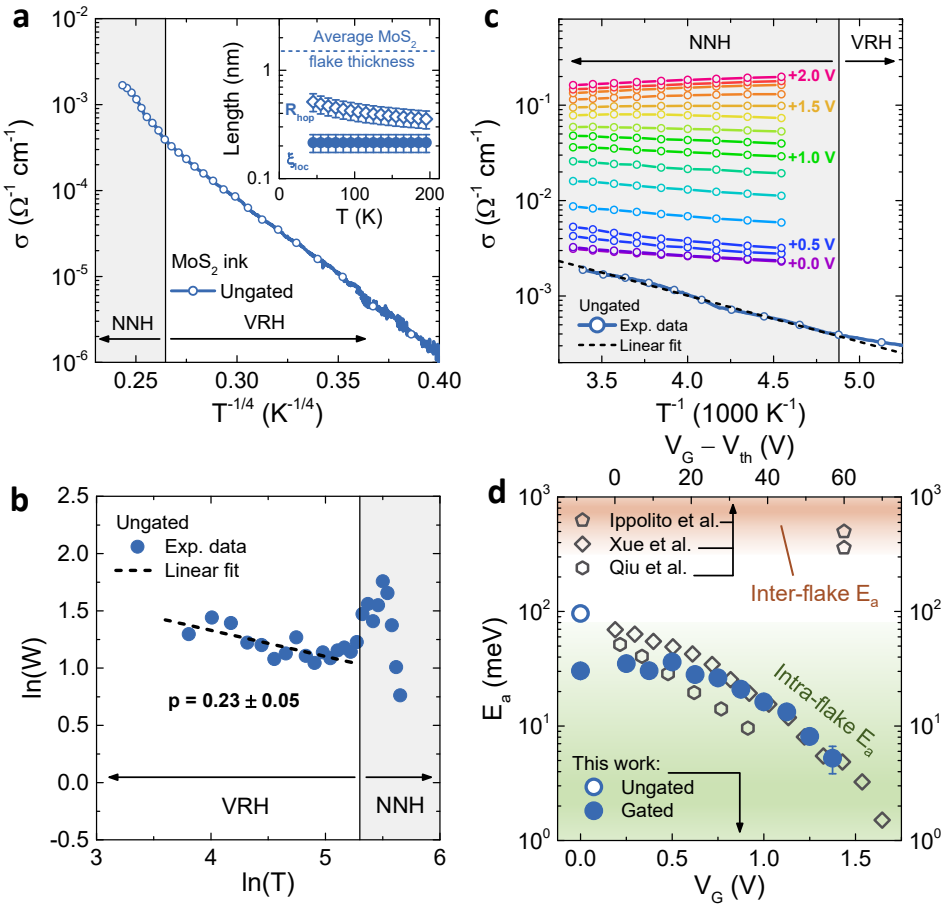

FIG. 4. Intra-flake hopping transport in printed MoS_2 devices. **a**, Conductivity σ as a function of $T^{-1/4}$ for an ungated MoS_2 device (blue solid line). Hollow symbols indicate the data points used to determine the reduced activation energy W shown in **b**. The grey shaded region highlights the T range ($T \geq 200\,\mathrm{K}$) where σ deviates from the $T^{-1/4}$ scaling due to the onset of NNH conduction. Inset: localization length ξ_{loc} (filled circles) and average hopping distance R_{hop} (hollow diamonds) as a function of T. The lengths are obtained combining the T-dependence of σ with the estimated values of $N(E_{\mathrm{F}})$ using Eq. 6. The horizontal dashed line highlights the average flake thickness in the MoS_2 ink. **b**, $\ln(W)$ as a function of $\ln(T)$ extracted from the numerical derivation of the data shown in panel **a**. The dashed black line is the linear fit to the data in the range $\ln(T) \leq 5$, which allows determining the corresponding value of the scaling exponent p. **c**, σ as a function of T^{-1}, for different values of the gate voltage V_{G}. The circles indicate the points used to determine the transfer curves in Fig. 3f. The blue curve refers to the ungated device, and the dashed black line is the linear fit to these data for $T \geq 200\,\mathrm{K}$, i.e. in the NNH regime (grey-shaded region). **d**, Activation energy E_{a} as a function of V_{G} (bottom scale) in different MoS_2 devices. Blue circles are obtained from the fit of the conductance curves of panel **c**. Black symbols are the values of E_{a} reported in disordered MoS_2 flakes (from Ref. 29, diamonds and Ref. 32, hexagons) and in MoS_2 networks (from Ref. 69, pentagons) as a function of the difference between the solid-gate voltage and the threshold voltage for electronic conduction (top scale).

$\log(\sigma_{\mathrm{MS}})$ scales linearly with $T^{-1/4}$ for $T \leq 200\,\mathrm{K}$, indicating of 3D-Mott VRH conduction [60–62]. ES-VRH, characterized by a $T^{-1/2}$ scaling of $\log(\sigma)$, is instead ruled out (see also Fig. S9). This is further confirmed by determining the reduced activation energy [72, 73]:

$$W(T) = \frac{\partial(\ln(\sigma))}{\partial(\ln(T))} \qquad (2)$$

Fig. 4b shows the values of $\ln(W_{\mathrm{MS}})$ for our MoS_2 device as a function of $\ln(T)$ (circles), and their linear fit for $\ln(T) \leq 5.3$ (dashed line) gives $p_{\mathrm{MS}} = 0.23 \pm 0.05$, in good agreement with $p = 1/4$ expected for 3D-Mott VRH.

On increasing T above 200 K, $\ln(W_{\mathrm{MS}})$ shows a peak and then decreases faster than below 200 K, leading to $p_{\mathrm{MS}} \geq 1$ and the onset of a different transport mechanism. For $T \geq 200\,\mathrm{K}$, $\log(\sigma_{\mathrm{MS}})$ (circles) scales with T^{-1} (Fig. 4c), indicating that the electric conduction occurs via NNH [60, 61]. Similar crossovers from Mott-VRH at low T to NNH at high T have been reported in disordered MoS_2 flakes [29, 32], although the VRH mechanism was invariably of the 2D-Mott type [29, 31, 32, 73]. Fitting σ_{MS} in the NNH region to Eq. 1 with $p = 1$ (dashed

line) gives $E_{a,MS} = 96.1 \pm 0.5$ meV for our ungated MoS_2 device. Fig. 4c also displays σ_{MS} for different values of V_G, and fitting these curves gives the V_G-dependence of $E_{a,MS}$, which ranges between ~ 4 and ~ 40 meV (blue circles in Fig. 4d). A positive $E_{a,MS}$ is obtained only for V_G up to 1.37 V, since for larger values of V_G, σ_{MS} decreases with increasing T and a negative $E_{a,MS}$ is obtained, again consistent with the charge transport occurring over extended states for $V_G \geq 1.37$ V and $T \geq 200$ K. The values of $E_{a,MS}$ in both our ungated and gated devices are comparable to those obtained in disordered, isolated MoS_2 flakes [29, 32] rather than to the much larger ones obtained in MoS_2 networks [69] where the conduction is dominated by inter-flake hopping (grey symbols).

We then determine the localization length ξ_{loc} and the average hopping distance R_{hop} in the VRH regime as a function of T (Eq. 6, see Methods) and compare them with the average thickness of the MoS_2 flakes, $t_{av,MS}$ (see the inset to Fig. 4a). We obtain $\xi_{loc,MS} = 0.21 \pm 0.04$ nm (filled circles), a value smaller than those found in ungated individual MoS_2 flakes, which range between 0.6 and 3.4 nm [29, 32, 73]. This is consistent with the stronger insulating behaviour exhibited by our printed MoS_2 devices, as also shown by $T_{0,MS} = (3.07 \pm 0.10) \cdot 10^6$ K (see Methods) being one order of magnitude larger than the values reported in ungated individual MoS_2 nanoflakes [29, 32]. $R_{hop,MS}$ (hollow diamonds) ranges from ~ 0.3 nm at 200 K to ~ 0.5 nm at 45 K thus remaining smaller than $t_{av,MS}$ in the entire T range. On average, an electron will thus hop multiple times before being able to escape each MoS_2 flake in the out-of-plane direction, accounting for how a 3D VRH can be observed even when the flakes are quasi-2D and the rate-limiting step is *intra*-flake hopping, consistent with the observed values of $E_{a,MS}$. This picture is in agreement with the observed distribution of flake orientations in the MoS_2 device (see Fig. S10), that demonstrates a fairly good alignment to the SiO_2 substrate, with a small average relative inclination of $\theta_{MS} < 3°$. This, together with the rather large lateral size of the flakes and their small average thickness, suggests an inkjet-printed film with high degree of alignment between the MoS_2 flakes with a good inter-flake connectivity in which, however, the conductivity is dominated by an intra-flake mechanism of conduction.

Overall, the charge transport in our inkjet-printed MoS_2 devices is dominated by intra-flake hopping processes. Ungated devices sit deep in the insulating side of the IMT, and exhibit a crossover from 3D-Mott VRH conduction for $T \leq 200$ K to NNH conduction for $T \geq 200$ K. Gated devices, on the other hand, exhibit NNH conduction for $T \geq 200$ K up to $V_G \sim 1.37$ V, and an incipient crossover to a high-T conduction over extended states for larger values of V_G.

HOPPING TRANSPORT IN INKJET-PRINTED GRAPHENE DEVICES

The increase of σ_{GR} with T in the printed graphene devices is qualitatively different from the behaviour of isolated graphene flakes, already suggesting that the bottleneck for electric transport is interflake hopping. Fig. 5a shows that $\log(\sigma_{GR})$ scales linearly with $T^{-1/4}$ for $V_G = 0, \pm 80$ V (red, green and brown curves) up to $T \sim 290$ K, again meaning that a 3D-Mott VRH mechanism [60–62] is at play over the entire T range. Fitting the data to Eq. 1 with $p = 1/4$ gives $T_{0,GR} = 138 \pm 11$ K, which is smaller than room temperature. This is commonly observed in networks composed of metallic grains when the charge transport is dominated by insulating inter-grain hopping [62, 70, 74], and indicates that the printed graphene device is very close to the IMT [74, 75]. Indeed, in granular systems the inter-grain energy barrier is set by the presence of a finite inter-grain capacitance, and VRH behaviour can be observed when electrostatic disorder lifts the Coulomb blockade and leads to a finite DOS at the Fermi level [62]. The T-dependence of $\log(\sigma_{GR})$ is also incompatible with the $T^{-1/2}$ scaling of ES-VRH (Fig. S9). Therefore, the 3D-Mott VRH mechanism observed in our devices differs from the hopping behaviour reported in defective graphene (falling either in the ES-VRH regime [76] or in the 2D-Mott VRH regime [77, 78]), but also from the metallic behaviour usually exhibited by crystalline single- and few-layer graphene flakes [33–35], and from the hopping behaviour observed in inkjet-printed graphene/polymer composites (NNH dominated by inter-flake capacitive charging) [65, 79] and spin-coated reduced graphene oxide (ES-VRH) [72].

Fig. 5b shows $\ln(W_{GR})$ as a function of $\ln(T)$ for $V_G = 0, \pm 80$ V (red, green and brown symbols), which is not monotonic and displays a slope change at $\ln(T) \sim 5.3$ ($T \sim 200$ K). Linearly fitting the data for $2 \leq \ln(T) \leq 5$ (dashed line) gives $p_{GR} = 0.26 \pm 0.01$ irrespective of V_G. Above 200 K, i.e. $\ln(T) \geq 5.3$, W_{GR} increases with increasing T, indicating that the charge transport deviates from the pure VRH scaling, as already suggested by $\mu_{FE,GR}$ decreasing with T in the same T range (Fig. 3g). $T \geq 200$ K thus marks the range where σ_{GR} is no longer limited purely by the carrier hopping probability and e-ph scattering is no longer negligible [33, 34]. The dimensionality of the VRH in the graphene devices is affected by the flake orientation: devices printed on SiO_2 display 3D-VRH and feature a rather large average relative inclination of the flakes with respect to the substrate ($\sim 14°$, see Fig. S10). Instead, flexible graphene films printed on PET exhibit 2D-VRH with $p_{GR} = 0.38 \pm 0.02$ (Fig. S11) and cross-sectional TEM analysis shows their flake stacking having a more pronounced in-plane orientation (Fig. S12). The geometry of the printed flake network thus sets the dimensionality of the VRH processes, meaning that inter-flake hopping dominates the conduction of inkjet-printed graphene devices.

This picture is further informed by determining the values of ξ_{loc} and R_{hop} a function of T (Eq. 6, see Methods). Fig. 5d shows that $\xi_{loc,GR} \sim 13$ nm (red circles) is nearly independent on T and much larger than that in

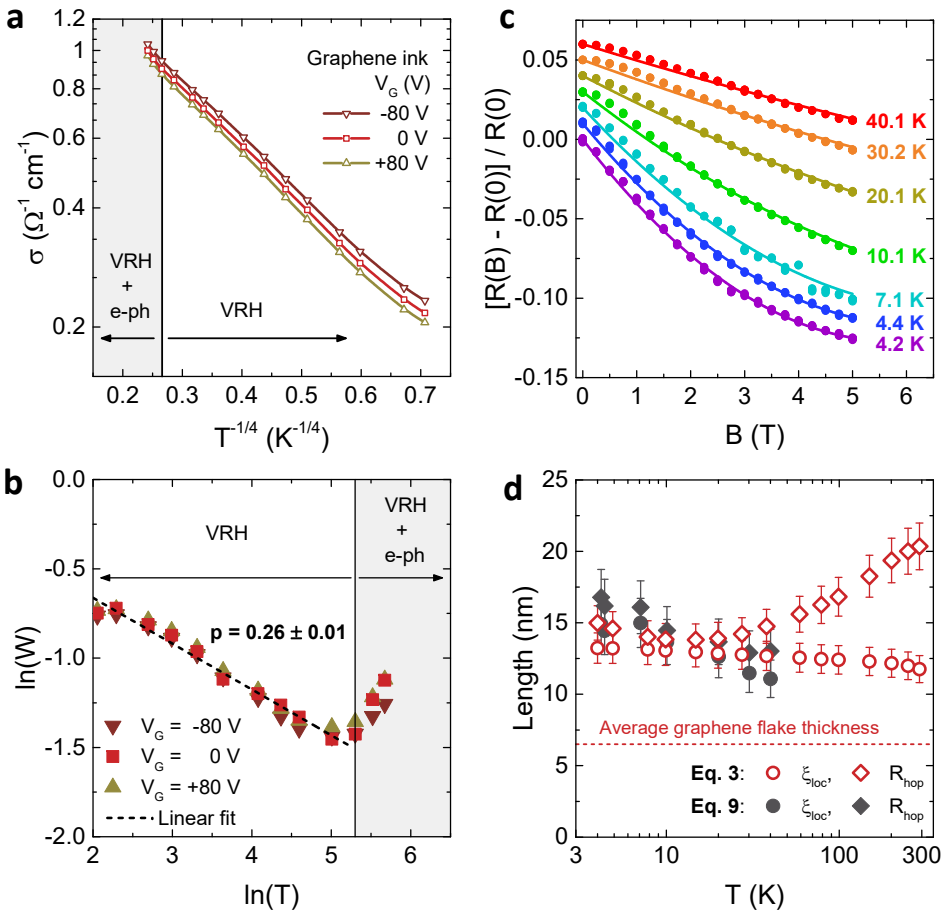

FIG. 5. Inter-flake hopping transport in printed graphene devices. **a**, Conductivity σ as a function of $T^{-1/4}$ for a printed graphene device at $V_G = -80$ V (brown solid line and hollow down triangles), $V_G = 0$ V (red solid line and hollow squares) and $V_G = +80$ V (yellow solid line and hollow up triangles). Hollow symbols are the data points used to determine the reduced activation energy W shown in **b**. The grey shaded region highlights the T range where a non-negligible contribution from e-ph scattering is present. **b**, $\ln(W)$ as a function of $\ln(T)$ extracted from the numerical derivation of the data shown in panel **a**. The dashed black line is the linear fit to the data in the range $2 \leq \ln(T) \leq 5$, which allows determining the corresponding values of the scaling exponent p. **c**, Magnetoresistance ratio $[R(B) - R(0)]/R(0)$ as a function of the magnetic field B at different temperatures. Filled circles are the experimental data, solid lines are the fits according to Eq. 9. Curves at different T are vertically offset by 0.01 for clarity. **d**, Localization length ξ_{loc} (circles) and average hopping distance R_{hop} (diamonds) as a function of T in the printed graphene device. The lengths indicated with red hollow symbols are obtained combining the T-dependence of σ with the estimated values of $N(E_F)$ using Eq. 6; those indicated by black filled symbols are instead obtained combining the T-dependence of σ with the MR fits of panel **c** using Eq. 9. The horizontal line highlights the average flake thickness in the graphene ink.

the MoS_2 devices, consistent with the more conductive behaviour of the graphene devices. $R_{hop,GR}$ shows a non-monotonic temperature dependence (red diamonds): For $T < 40$ K, it slightly decreases with increasing T, going from $R_{hop,GR} \sim 16$ nm to $R_{hop,GR} \sim 13$ nm; for $T > 40$ K instead it slowly increases, reaching $R_{hop,GR} \sim 20$ nm close to room T. This behaviour can be ascribed to the fact that, in this case, $T_{0,GR}$ is smaller than room T and the factor F_0 in Eq. 7 (see Methods) becomes relevant as T approaches and exceeds $T_{0,GR}$. Most importantly, in the graphene devices $R_{hop,GR}$ is systematically larger than the average flake thickness $t_{av,GR}$ for any T, consistent with carrier hopping occurring primarily between different graphene flakes in the 3D network. These results are confirmed by measuring the magnetoresistance ratio $MR = [\rho(B) - \rho(0)]/\rho(0)$, which in the VRH regime directly probes ξ_{loc} [80] (see Methods). Here $\rho = \sigma^{-1}$ is the resistivity of our graphene devices and B is the magnetic field. Fig. 5c shows the experimental values of MR as a function of B (symbols), measured with B in the out-of-plane direction at temperatures between 4.2 K and 40.1 K. The solid lines represent the best fit to our experimental MR data using Eq. 9 (see Methods). The MR is always negative, quasi-linear at low B, with an incipient saturation at high B for $T \leq 20$ K. Such a behaviour is typical of MR in the VRH regime [80], which is

determined by the sum of a linear ($\propto B$) and a quadratic ($\propto B^2$) contribution arising from the quantum interference of different hopping paths and the contraction of the charge-carrier wavefunction at impurity centres, respectively [80]. Our fits with this model show an excellent agreement with the experimental data. Fig. 5d shows the values of $\xi_{\mathrm{loc,GR}}$ (black circles) and $R_{\mathrm{hop,GR}}$ (black diamonds) obtained from the best fits of the MR data in Fig. 5c. Both $\xi_{\mathrm{loc,GR}}$ and $R_{\mathrm{hop,GR}}$ are $\sim 15\,\mathrm{nm}$ at 4.3 K and decrease to $\sim 11\,\mathrm{nm}$ and $\sim 13\,\mathrm{nm}$ at 40.1 K respectively, in excellent agreement with the values determined from Eq. 6. Overall, the charge transport in our inkjet-printed graphene devices is thus fully described in terms of a Mott VRH conduction dominated by inter-flake hopping processes, on the verge of an IMT for $T \geq T_{0,\mathrm{GR}}$.

WEAKLY-LOCALIZED TRANSPORT IN INKJET-PRINTED MXENE DEVICES

Fig. 6a shows ρ as a function of T for a printed MXene device (green curve) as compared to that of MXene film of comparable thickness epitaxially grown on sapphire (Ref. 63, black curve). The ρ of the printed film is about one order of magnitude larger than that of the epitaxial film (at $T = 290\,\mathrm{K}$, $\rho \sim 47.6$ and $5.86\,\mu\Omega\,\mathrm{m}$ respectively), indicating that the printed film is more disordered than the epitaxial film. In both cases ρ depends only weakly on T, in full contrast with the exponential dependence observed in the printed graphene and MoS_2 films, and in line with the typical behaviour of a disordered metallic system [60–62]. For $T \geq 100\,\mathrm{K}$, ρ increases with increasing T, a fingerprint of conduction occurring over extended states when e-ph scattering is activated by the increasing T [60–62]. For $T \leq 100\,\mathrm{K}$, ρ exhibits a minimum at $T \sim 80\,\mathrm{K}$ and increases again with decreasing T (Fig. 6a). Such a low-T upturn is typical of disordered 2D metals [35, 81, 82] and was also observed in isolated Ti_3C_2 flakes [36], epitaxial films [63] and spray-casted networks [71], strongly pointing to a common charge transport mechanism in all these systems. A mainly 2D charge transport is rather reasonable in our MXene devices due to the large lateral size and small thickness of the flakes, together with an excellent substrate conformality, with a narrow distribution of their average relative inclination peaked at $\theta_{\mathrm{max,MX}} \sim 0.63°$ (Fig. S10).

Fig. 6b shows that $\sigma_{\mathrm{s}} = \sigma \cdot t_{\mathrm{d,MX}}$ (green line) is proportional to $\log(T)$ in the range $7\,\mathrm{K} \leq T \leq 70\,\mathrm{K}$ (dashed line), as usually observed in disordered 2D conductors [35, 81, 82], or in granular metals where the inter- and intra-grain conductances are comparable [62]. However, in the latter case the fully-metallic T-dependence we observe experimentally for $T \geq 100\,\mathrm{K}$ cannot develop [62]. Considering that the same behaviour was observed in isolated flakes [36] and epitaxial films [63], and that the ratio (η) of the proportional change of $d\rho/dT$ to the proportional change in ρ due to the gate-induced doping is positive (Fig. S13) [71], we thus treat our printed MXene devices as granular 2D metals where the *intra*-grain conductance dominates. The logarithmic scaling of σ_{s} with T can then be due to three distinct phenomena (or a combination thereof) [35, 81, 82]: Kondo effect, electron-electron interactions (EEI) and weak localization (WL). Among these, in epitaxial MXene thin films WL has been proposed to be responsible for the upturn of ρ occurring at low T [63].

These phenomena each feature a unique dependence of the magnetoconductance $\Delta\sigma(B,T) = \sigma_{\mathrm{s}}(B,T) - \sigma_{\mathrm{s}}(0,T)$ on B due to their distinct physical origin, as detailed in the Supplementary Section XVI. Fig. 6c shows that at any T between 4.3 K and 40 K, our MXene devices exhibit a finite and positive $\Delta\sigma(B)$ (filled circles), ruling out the B-independent EEI as a major source for the ρ upturn [35, 81, 82]. The $\Delta\sigma(B,T)$ is symmetric for positive and negative values of B (Fig. 6d), but even at $T = 4.2\,\mathrm{K}$ (violet circles) does not follow a quadratic behaviour in the low-field limit ($|B| \leq 2\,\mathrm{T}$) and cannot be fitted satisfactorily by a parabola (dashed line), thus excluding also Kondo effect as a source for the ρ upturn [83]. Fig. 6e shows the anisotropic magnetoconductance $\mathrm{AMC} = \sigma_{\mathrm{s}}(B,\theta) - \sigma_{\mathrm{s}}(B,0)$, where θ is the angle between B and the substrate plane. At any B, the experimental AMC data (filled circles) closely follow the $\sin(\theta)$ dependence expected for a 2D Fermi surface [84] (solid lines), and the positive $\Delta\sigma(B,T)$ observed upon the application of an out-of-plane B ($\theta = 90°$) is entirely suppressed when B is applied in-plane ($\theta = 0°$), as expected in the case of 2D WL behaviour [35, 81, 82] (Fig. S14). Consistently with the findings on epitaxial MXene films [63], we thus attribute the source of the ρ upturn below $\sim 80\,\mathrm{K}$ to the presence of 2D WL, and analyse quantitatively our data employing the Hikami-Larkin-Nagaoka (HLN) model [85] (see Methods). The fits of the experimental $\Delta\sigma(B,T)$ values to Eq. 12 (solid lines in Fig. 6c) are in agreement with the experimental values of $\Delta\sigma(B)$ for all values of T. Charge transport in our MXene devices is thus well described in terms of WL in the presence of a finite spin-orbit interaction (SOI), with no qualitative differences with respect to epitaxial films [63].

Fig. 6f shows the phase-coherence length L_ϕ (red diamonds), the spin-orbit length L_{so} (black circles) and the elastic-scattering length L_{e} (green pentagons) determined from the fits in Fig. 6c (see Methods). $L_{\mathrm{e}} \sim 10\,\mathrm{nm}$ and nearly T-independent for $T \leq 10\,\mathrm{K}$, as expected for scattering with defects, and is comparable but larger than the mean free path $\sim 2\,\mathrm{nm}$ estimated at 300 K [45], due to e-ph scattering reducing the latter. L_ϕ decreases upon increasing T and scales as $T^{-1/2}$ (Fig. 6g), identifying Nyquist electron-electron scattering as the main source of dephasing in the system [35, 86]. L_{so} is constant with T, as typical for 2D conductors with finite SOI [86], and larger than both L_ϕ and L_{e} at any T, indicating that SOI is unable to induce a complete spin precession in the charge carriers before they lose phase coherence; this would destroy the constructive interfer-

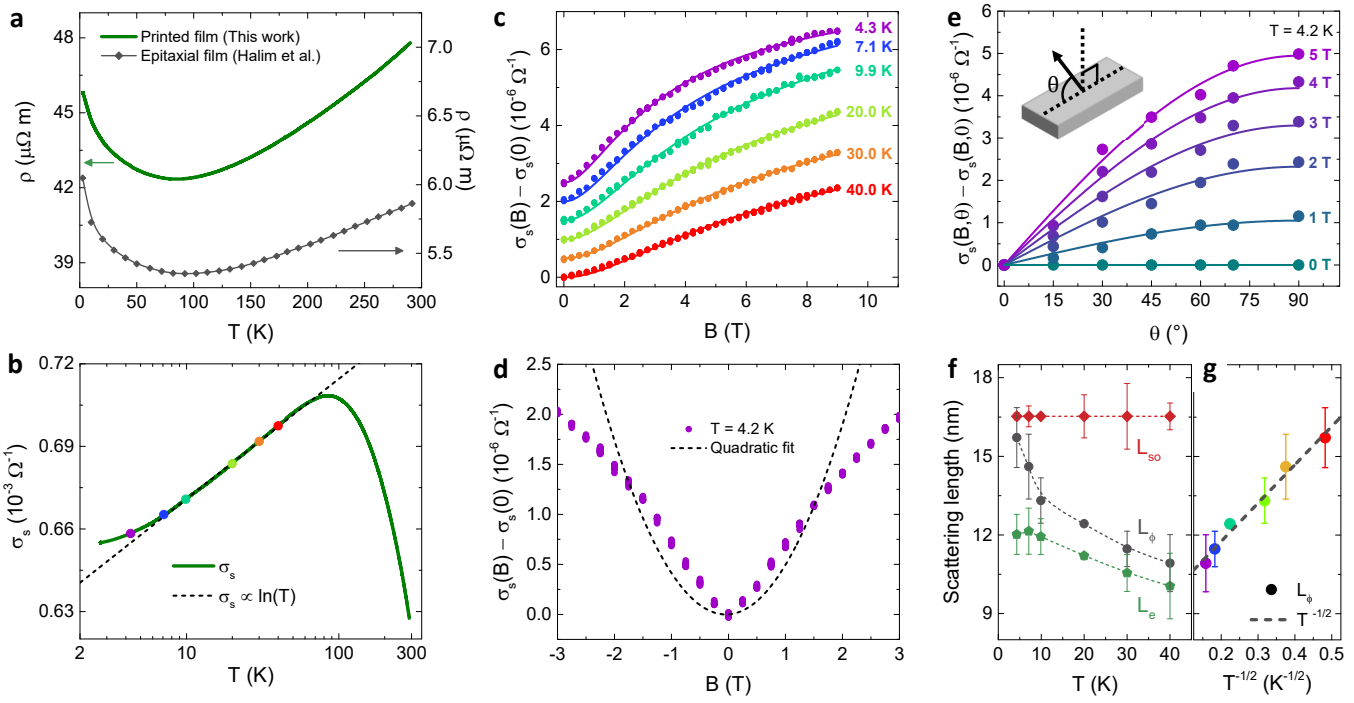

FIG. 6. Intra-flake metallic transport in printed MXene devices. **a**, Resistivity ρ as a function of T for a printed MXene device (solid green line, left scale) compared to that of an epitaxial MXene film from Ref. 63 (black solid line and filled diamonds, right scale). **b**, Same data of panel **a** for the printed MXene device, plotted as conductivity per unit surface σ_s as a function of $\log(T)$ (solid green line). The dashed black line is a linear fit to the data. Filled coloured circles mark the values of T at which the B sweeps shown in panel **c** were acquired. **c**, Magnetoconductance $\sigma_{2D}(B) - \sigma_{2D}(0)$ as a function of the intensity B of the magnetic field (perpendicular to the film), for increasing temperatures. Filled circles are the experimental data, solid lines are the fits according to Eq. 12. Curves at different T are vertically shifted by $5 \cdot 10^{-7}\,\Omega^{-1}$ for clarity. **d**, $\sigma_{2D}(B) - \sigma_{2D}(0)$ as a function of B (perpendicular to the film) for low positive and negative values of B. Violet circles are the experimental data at $T = 4.3\,\mathrm{K}$, the black dashed line is a quadratic fit to the data for $-2\,\mathrm{T} \leq B \leq +2\,\mathrm{T}$. **e**, Anisotropic magnetoconductance as a function of the angle θ between B and the substrate plane, for different values of B. Filled circles are the experimental data at $T = 4.2\,\mathrm{K}$. Solid lines are fits to $\sin(\theta)$ dependencies. **f**, Spin-orbit length L_{so} (red diamonds), phase-coherence length L_ϕ (black circles) and elastic scattering length L_e (green pentagons) as a function of T, as determined from the fits to Eq. 12 shown in panel **c**. Dashed lines are guides to the eye. **g**, L_ϕ as a function of $T^{-1/2}$ (filled coloured circles) and a linear fit to the data (black dashed line).

ence responsible for WL and lead to the appearance of weak anti-localization (WAL), and no WAL-induced negative magnetoconductance close to $B = 0$ is observed in Fig. 6c,d, in agreement with the results on MXene epitaxial films [63]. Moreover, at $T = 4.3\,\mathrm{K}$, L_ϕ is approaching L_{so}, accounting for the incipient saturation of σ_s observed for $T \leq 7\,\mathrm{K}$ due to reduced constructive interference (see Supplementary Section XVI). Since L_ϕ, L_{so} and L_e remain much smaller than the average lateral size of the MXene flakes, the WL behaviour in our printed MXene devices is fully determined by phase-coherent *intra*-flake charge transport.

CONCLUSIONS

We successfully identified and described the charge transport mechanisms of thin-film field-effect devices made from representative few-layer E2D inks (semiconducting MoS_2, semimetallic graphene and metallic Ti_3C_2 MXene), fabricated by direct inkjet-printing on SiO_2/Si substrates. We investigated their electrical conductivity as a function of temperature, magnetic field and gate voltage, accounting for morphological features of the flakes and the printed films. We demonstrated that the charge transport in the printed MoS_2 and MXene devices is dominated by the intrinsic *intra*-flake processes, leading to a temperature-induced crossover between 3D-Mott variable-range hopping and nearest-neighbour hopping in the former, and a weakly-localized metallic behaviour in the latter. In the printed graphene devices, we demonstrated that the charge transport is determined by *inter*-flake processes, leading to a variable-range hopping behaviour up to room temperature in spite of the semimetallic nature of the single flakes, and resulting in a strong dependence of the dimensionality of the charge

transport on that of the flake network in the printed film. Our findings establish the fundamental mechanisms responsible for charge transport in inkjet-printed devices made of E2D inks, and pave the way for a reliable design of more complex printed electronics with E2D inks.

METHODS

Graphene ink preparation. The graphene ink was prepared by a surfactant-free liquid-phase exfoliation of graphite using a high-boiling-point solvent which was then solvent-exchanged into a low-boiling-point solvent, thus minimising solvent residuals. The use of a low-boiling-point solvents aids at preventing the coffee-ring effect hence creating a uniform film. In addition we used a low-boiling-point solvent which is non-toxic and does not damage the inkjet-printer cartridge (piezoelectric-based printhead) during the printing process. An initial 1.5 g of Sigma Aldrich (Sigma-Aldrich No. 332461, size $< 100\,\mu$m) graphite was added to 150 ml of NMP and ultrasonicated (Fisherbrand FB15069, Max power 800 W) for 9 hrs. The graphite-NMP ink was subsequently centrifugated (Sorvall WX100 mounting a TH-641 swinging bucket rotor) for 1 hr at 10,000 rpm. The supernatant was transferred into a clean glass bottle using a micropipette. Great care was taken during pipetting to avoid the disturbance of the sediment layer which could re-disperse into the supernatant. The solvent exchange was carried out via vacuum filtration, where 20 ml of graphene ink was passed through a PTFE membrane (Merck Millipore, 0.1 µm). Graphene collected on the PTFE membrane was transferred to a small vial along with 5 ml of pure ethanol. This was followed by 10 min of ultrasonication. Printing was carried out immediately after the ink preparation.

Ti_3C_2 ink (MXene) preparation. The MXene ink was prepared by following the mild-exfoliation-route protocol for MAX phase powder (Ti_3AlC_2). This involves etching the Al atom in the MAX powder via the creation of in-situ hydrofluoric acid. As for the graphene ink, we also opted for a solvent-exchange route for the MXene ink by exchanging the high-boiling-point solvent to a benign low-boiling-point solvent. In a vented 40 ml PTFE vessel, deionised water (5 ml) was added, followed by drop-wise addition of concentrated hydrochloric acid (15 ml, Sigma). LiF powder (1 g, Sigma) was added to the resultant 9M HCl, and the vessel was then immersed in a mineral oil bath at 35 °C and stirred using a magnetic PTFE bar for 10 min to fully dissolve the LiF and allow the temperature to stabilise. Ti_3AlC_2 MAX phase powder (1 g, Carbon-Ukraine ltd.) was then added in small additions to the vessel to avoid overheating of the solution. The solution was then left stirring for 24 hours to obtain the etched, multilayer $Ti_3C_2T_x$ MXene. The contents of the vessel were transferred into a 50 ml centrifuge tube and diluted to a total of 40 ml with deionised water. The dispersion was then sedimented via centrifugation at 5000 rpm using a Thermo Scientific Heraeus Multifuge X1 for 5 min, discarding the supernatant and repeating several times, until the pH of the supernatant was 6. To delaminate the washed multilayer MXene, the tube was sealed tightly and shaken vigorously by hand and vortex mixing for 30 min. The dispersion was then centrifuged at 1500 rpm for 30 min to sediment any many-layer MXene or unreacted MAX phase. The supernatant containing delaminated MXene flakes was then collected. For ease of printing, the dispersion was transferred into NMP (Sigma Aldrich) via centrifugation at 5000 rpm, redispersing the sediments in minimal NMP and repeating three times to remove remaining water. To obtain a printable MXene dispersion in ethanol, the NMP ink was transferred via centrifugation, repeating 3 times with absolute ethanol (5 ml, Fisher Scientific). The resulting dispersion was sonicated for 15 min to break up agglomerated flakes and then centrifuged at 2500 rpm for 30 min to remove any remaining agglomerates. The supernatant was collected for use in inkjet printing.

MoS_2 ink preparation. The MoS_2 ink was prepared by following the electrochemical exfoliation route which involved the intercalation of quaternary ammonium bromide in between the bulk MoS_2 layers. The electrochemical set up involved using a natural MoS_2 crystal (HQ graphene) and a graphite rod (Qingdao Tennry Carbon Co.) as the cathode and anode respectively. The electrolyte was made by adding 0.2 g of quaternary ammonium bromide (Sigma-Aldrich, CAS number: 4368-51-8, SKU: 87301) to 40 ml of acetonitrile giving a concentration of $5\,\mathrm{mg\,ml^{-1}}$. Both the MoS_2 crystal and graphite electrode were submerged in the quaternary ammonium bromide electrolyte and the applied voltage was set at 8 V for 1 hr. The expanded MoS_2 crystal was washed with ethanol and then broken up into smaller pieces. The small pieces of MoS_2 were transferred to a test tube and Dimethylformamide (DMF) with Polyvinylpyrrolidone (PVP) ($22\,\mathrm{mg\,ml^{-1}}$, Sigma-Aldrich, CAS Number 9003-39-8, SKU: PVP40, Molecular weight $\sim 40,000$) was added to the test tube and the mixture was sonicated for 30 min. The mixture was then broken down further using a shear mixer (IKA-T10). The dispersion was then centrifuged at 3000 rpm for 20 min to remove any large piece of MoS_2 that was not electrochemical exfoliated. The supernatant was then centrifuged again at 5000 rpm for 10 min to futher separate few-layer MoS_2 flakes from bulk MoS_2. Both centrifuge steps were performed using a ProteomeLab^{TM} XL-A by Beckman Coulter along with a SW 32 Ti Swing-Bucket rotor. The supernatant of the second centrifuge step was placed under a vacuum line ($\sim$ 1 mbar) to remove the DMF solvent and concentrate the MoS_2 ink. The concentrate dispersion, which had a volume of 10 ml, was centrifuged at 45,000 rpm for 30 min to sediment the MoS_2 flakes. This centrifuge step was performed using a Beckman Optima MAX Ultracentrifuge. The sediment MoS_2 was re-dispersed in isopropyl alcohol (IPA) with PVP ($22\,\mathrm{mg\,ml^{-1}}$). The MoS_2 dispersed in IPA was directly used to print the MoS_2 film with no further processing required.

Transmission electron microscopy. Transmission electron microscopy (TEM) was performed using a FEI Philips Tecnai F-20 operated at 200 kV (Tungsten, LB6) with a line resolution of 0.10 and point resolution of 0.24 nm. The TEM sample were prepared by diluting the initial E2D ink by a factor of 100 and drop casting the diluted solution on holey carbon film 400 mesh copper (Cu) grid which was then allowed to dry in ambient air overnight.

Ink Jet printing. Before performing the printing process, each Si/SiO_2 substrate (Graphene supermarket 285 nm p-doped) was treated with ozone plasma (NanoBioAnalytics UV Ozone Cleaner UVC-1014) to make the surface more hydrophilic. A drop-on-demand ink-jet printer (Fujifilm Dimatix DMP-2800) with a nozzle diameter of 21 µm that produce droplets with a volume of $\sim$ 10 pl was used to print the devices. The E2D inks were made using low-boiling-point solvents (< 100°C) which evaporate at room temperature hence minimising both the transport of particulates (causing "coffee rings") and the re-dispersion of the material, thus improving the morphological uniformity of the film.

Rheology. A rotational rheometer (Discovery Hybrid Rheometer HR-1) that uses a parallel plate method to measure the viscosity and viscoelastic properties of a liquid was used to characterize all the inks employed in this work. Shear-thinning was observed in all the inks. The surface tension of the inks was measured using pendant drop method (First Ten Angstroms FTA1000B). Built-in software analysed the shape of the suspended droplet formed at the end of the needle via drop shape analysis (DSA). Ink density (ρ) was measured by weighing 1 ml of ink on a microbalance (Sartorius ME5). The density of the inks was determined as $\rho = m/V$ where m and V are the mass and volume respectively. All inks were formulated with surface tension

$\gamma \sim 29\,\mathrm{mN\,m^{-1}}$ and viscosity $\eta \sim 1\,\mathrm{mPa}$ (see Figs. S5 and S6). The corresponding density of the inks is $\rho_{GR} \sim 0.8\,\mathrm{g\,cm^{-3}}$, $\rho_{MS} \sim 0.7\,\mathrm{g\,cm^{-3}}$ and $\rho_{MX} \sim 0.99\,\mathrm{g\,cm^{-3}}$ for the graphene, MoS_2 and MXene inks, respectively. The Ohnesorge number (a dimensionless number that relates the viscous forces to inertial and surface tension forces) was determined as $\mathrm{Oh} = \eta/\sqrt{\rho\sigma L}$, where L is the diameter of the nozzle, and the corresponding figure of merit $\mathrm{Z} = \mathrm{Oh}^{-1}$ was derived.

Optical absorption spectroscopy. The flake concentration c of the graphene, MXene and MoS_2 inks was determined using the Beer-Lambert law $A = \alpha c l$, where c is the concentration, l is the beam path length and α is the absorption coefficient. For the latter, we used the values at 660 nm $\alpha_{660(GR)} \sim 2460\,\mathrm{L\,g^{-1}m^{-1}}$ for the graphene ink [12], $\alpha_{660(MX)} \sim 538\,\mathrm{L\,g^{-1}m^{-1}}$ for the MXene ink (see also Fig. S15) and $\alpha_{672(MS)} \sim 3400\,\mathrm{L\,g^{-1}m^{-1}}$ for the MoS_2 ink.

Raman spectroscopy. A Renishaw 1000 InVia micro-Raman spectrometer was used to acquire the Raman spectra. The spectra shown in Fig. 2 were measured using a 514 nm laser with an 20x objective. All the Raman spectra were acquired using a laser power of $\sim 1\,\mathrm{mW}$.

Atomic force microscopy. Inks were diluted by a factor of 100, then drop casted on pieces of Si/SiO_2 wafers and allowed to dry in ambient air. A short annealing step of 1 min at the boiling temperature of the solvent used to make the E2D ink, was performed before acquiring the AFM images. AFM measurements were performed using a Bruker Dimension icon with peakforce mode using a silicon tip on a Nitride lever.

X-ray photoelectron spectroscopy of the graphene ink and MoS_2 ink. A K-Alpha$^+$ surface analysis by Thermo Scientific was used to carry out measurements on all the inkjet-printed devices on SiO_2. A spot size of $200 - 400\,\mu\mathrm{m}$ was used for all the samples. The spectra were obtained in vacuum at a pressure $< 8{\cdot}10^{-7}\,\mathrm{mbar}$. The system employs a microfocused Al Kα X-ray source (1486 eV) and a 2D detector attached to a 180 double-focusing hemispherical analyser. Further analysis of the XPS spectra was carried out using the Avantage software by Thermoscientific.

X-ray photoelectron spectroscopy of the Ti_3C_2 ink. XPS spectra were recorded from an Omicron EA125 energy analyser (Scienta Omicron), using an XM1000 monochromated Al K X-ray source. The instrument's base pressure was $2 \cdot 10^{-10}$ mbar and the instrumental resolution was 0.6 eV. The spectra were deconvoluted and fitted using CasaXPS (Casa Software).

Device fabrication. All E2D ink devices were produced by using 25 printing passes. In the printed MoS_2 devices, we submerge our devices in bis(trifluoromethane)sulfonimide (TFSI) in 1,2-dichloroethane at 100 °C for 1 h. The treatment is performed in a nitrogen glovebox to avoid exposing TFSI to moisture in ambient atmosphere [66]. The devices are then annealed at 400 °C for 1 h to remove any residual solvent. We then created a thin gate oxide suitable for electric-field modulation. Electron-beam lithography was used to pattern $\sim 1\,\mathrm{mm}$ long source, drain and gate electrodes on Si/SiO_2 substrate. We use Ti/Au (5/35 nm) for the source and drain and Al (40 nm) for gate electrode of the FET. A thin native AlO_x layer was formed at the top surface of Al by air exposure (the gate length is $\sim 600\,\mathrm{nm}$ and the width $\sim 400\,\mu\mathrm{m}$).

Charge transport measurements. The electrical connections for charge transport measurements were realized by placing thin Au wires on the SiO_2/Si substrates close to the printed devices and then drop-casting small ($\sim 100\,\mu\mathrm{m}$) droplets of electrically-conducting Ag paste (RS components). Temperature-dependent charge transport measurements were performed in the high-vacuum chamber of a Cryomech pulse-tube cryocooler with a base temperature of 2.8 K. Magnetic-field dependent measurements were performed in He atmosphere in the variable-temperature insert of an Oxford Instruments ^{4}He cryostat equipped with a 9 T superconducting magnet. The conductivity of the printed devices was determined as:

$$\sigma = \frac{l}{w t_d}\frac{I}{V} \tag{3}$$

where l is the channel length, w its width, t_d is the device thickness, I the current flowing through the channel and V the voltage drop across it. The nearly linear scaling of σ_{GR} and σ_{MX} with V_G for both the graphene and MXene printed devices (see also Fig. S7) at any T for $|V_G| \leq 40\,\mathrm{V}$, allowed to determine the field-effect mobility μ_{FE} in both devices as:

$$\mu_{FE} = \frac{t_d}{C_G}\left|\frac{\partial\sigma}{\partial_G}\right| \tag{4}$$

and the average density of free carriers per unit volume at $V_G = 0$, $n_{3D}|_0$, as:

$$n_{3D}|_0 = \frac{\sigma(V_G = 0)}{e\ \mu_{FE}} \tag{5}$$

where e is the elementary charge, $C_G = \varepsilon_{ox}\varepsilon_0/t_{ox}$ is the gate capacitance per unit area, ε_0 is the vacuum permittivity, and ε_{ox} and t_{ox} are the dielectric constant and thickness of the gate oxide respectively. For the printed MXene and graphene devices, $t_{ox} = 285\,\mathrm{nm}$ and $\varepsilon_{ox} = 3.9$ is the permittivity of SiO_2 [30], resulting in $C_G = 12.1\,\mathrm{nF\,cm^{-2}}$. For the printed MoS_2 devices, $t_{ox} \sim 37\,\mathrm{nm}$ and $\varepsilon_{ox} \sim 3.77$ as an effective-medium approximation of AlO_x and vacuum, resulting in $C_G \sim 95\,\mathrm{nF\,cm^{-2}}$ (see Ref. 66 for details.) For ion-gated MoS_2 devices, the same definition of μ_{FE} is employed except that the solid-oxide capacitance is substituted for the ionic-gate capacitance $C_G \sim 10.8\,\mu\mathrm{F\,cm^{-2}}$ determined by low-bias cyclic voltammetry [87] (see Supplementary Section XIX and Fig. S16). Additionally, the two clearly different slopes in the plot of σ_{MS} as a function of V_G observed in the ion-gated MoS_2 devices above and below $V_G \sim 1.37\,\mathrm{V}$ required a separate determination of $\mu_{FE,MS}$ for these two cases in the temperature range from $T \sim 300\,\mathrm{K}$ to $T \sim 220\,\mathrm{K}$.

The printed MXene and graphene devices were measured in the four-probe configuration by supplying a small constant current $I_D \sim 1\,\mu\mathrm{A}$ between the outer drain (D) and source (S) contacts with a two-channel Agilent B2912 source-measure unit (SMU), and measuring the longitudinal voltage drop V_{xx} between the inner voltage contacts with an Agilent 34420 nanovoltmeter. Common-mode offsets were removed by the current reversal method. The gate voltage $-80\,\mathrm{V} \leq V_G \leq +80\,\mathrm{V}$ was applied between the S contact and the p-doped Si back gate with the same two-channel SMU. The printed MoS_2 devices were too resistive for the four-probe method to be reliable, and were thus measured in the two-probe configuration with a Keithley 2636B SMU by linearly sweeping V_D from $-0.1\,\mathrm{V}$ to $+0.1\,\mathrm{V}$, measuring the resulting I_D, and performing a linear fit to the data. All the measured IV curves in the printed MoS_2 devices showed a linear behaviour, indicating Ohmic contacts to the sample, and the contact resistance was determined to be negligible with respect to the total resistance of the device (see Fig. S17). In the printed MoS_2 devices in the absence of the ionic gate, $-1.5\,\mathrm{V} \leq V_G \leq +1.5\,\mathrm{V}$ was applied to the Al/AlO_x gate and an effective width w equal to 10% the apparent one was employed in the calculations, owing to the c-AFM measurements indicating that only a 10% fraction of the MoS_2 flakes were electrically connected to the Au leads. When the ionic gate was applied, we tuned σ_{MS} at low T by scanning V_G in 0.125 V steps between 0 and +2 V. At each step, a waiting time of $\sim 10\,\mathrm{min}$ minimised the influence of diffusion dynamics of the ions inside the MoS_2 film. We recorded the T dependence of σ_{MS} between 300 K and 220 K, below which the channel integrity was compromised by the freezing of the ionic liquid.

Calculation of the localization and average hopping lengths. For 3D-Mott VRH, the localization length ξ_{loc} is related

to the characteristic temperature T_0 as [60, 61]:

$$T_0 = \frac{24}{\pi k_B N(E_F) \xi_{loc}^3} \quad (6)$$

where $N(E_F)$ is the DOS at the Fermi level E_F, and the average hopping length R_{hop} is simply [60, 75]:

$$R_{hop} = \frac{3}{8}\left(\frac{T_0}{T}\right)^{\frac{1}{4}} \xi_{loc}\, F_0 \quad (7)$$

where F_0 is a correction factor that describes the VRH regimes when the condition $T \ll T_0$ is not satisfied (see Fig. S18a).

For our printed MoS_2 devices, from the fit of the curve in Fig. 4a to Eq. 1 with $p = 1/4$, we obtain $T \ll T_{0,MS} = (3.07 \pm 0.10) \cdot 10^6$ K in the ungated case, resulting in $F_0 = 1$. $N(E_F)_{MS}$ can then be obtained from $E_{a,MS}$ in the NNH regime at $V_G = 0$ ($E_{a,MS} = 96.1 \pm 0.5$ meV), since $E_a^{-1} = N(E_F)a^3$ [60] where a is the minimum distance between hopping sites. From a statistics of the Raman spectra of the printed MoS_2 flakes (see Fig. S19), we determine the inter-defect length L_D and thus set $a = L_D \sim 1.54$ nm, in good agreement with previous reports ($a \sim 1.7$ nm [32]).

Since the printed graphene devices do not exhibit NNH behaviour in any temperature range, $N(E_F)_{GR}$ cannot be estimated by starting from the activation energy of NNH; rather, one can estimate $N(E_F)_{GR}$ by combining the average free carrier density per unit volume $n_{3D}|_{0,GR}$ shown in Fig. S8a, with the energy-dependence of the DOS in graphite as determined by *ab initio* density functional theory [88]:

$$n_{3D}|_0 = \int_{E_D}^{E_F} N(E)dE \quad (8)$$

where E_D is the energy of the Dirac point. The validity of this approach in our graphene devices can be confirmed by independently determining ξ_{loc} from the magnetic-field dependence of their resistivity, since measuring the magnetoresistance of a material in the VRH regime allows directly probing ξ_{loc} without having to make any assumption on its DOS [80]. As discussed below, in the case of 3D-Mott VRH and in the low magnetic field limit ($B \ll B_{sat}, B_c$) the magnetoresistance ratio $MR = [\rho(B) - \rho(0)]/\rho(0)$ takes a specific field dependence given by Eq. 9, containing ξ_{loc} as a parameter.

Magnetoresistance and magnetoconductance fits. The magnetoresistance curves of the printed graphene device shown in Fig. 5e were fitted to the standard expression for hopping transport [80]:

$$MR = -C_{sat}\frac{B}{B_{sat}} + t^2\frac{B^2}{B_c^2} \quad (9)$$

Here, B_{sat} and B_c are characteristic values of B related to the localization length ξ_{loc}:

$$B_{sat} = 0.7\left(\frac{8}{3}\right)^{\frac{3}{2}}\left(\frac{2\pi\hbar}{e\xi_{loc}^2}\right)\left(\frac{T}{T_0}\right)^{\frac{3}{8}} \quad (10)$$

$$B_c = \frac{6\hbar}{e\xi_{loc}^2}\left(\frac{T}{T_0}\right)^{\frac{3}{8}} \quad (11)$$

where C_{sat} is the positive saturation constant [80], $t^2 = 0.0893$ is a numerical coupling constant [80], and $\hbar$ is the reduced Planck constant. The corresponding values of B_{sat} and B_c were found to be always larger than 17 T and 8 T respectively, validating the choice of the low magnetic field limit.

Conversely, the magnetoconductance curves of the printed MXene device shown in Fig. 6 were fitted to the Hikami-Larkin-Nagaoka model, which describes the magnetoconductance of 2D metallic systems in presence of finite intrinsic SOI [86]:

$$\Delta\sigma(B) = \frac{e^2}{2\pi^2\hbar}\left[F\left(\frac{B_\phi}{B}\right)\right] + \frac{e^2}{2\pi^2\hbar}\left[F\left(\frac{B_{so}+B_e}{B}\right)\right] - \frac{3e^2}{2\pi^2\hbar}\left[F\left(\frac{(4/3)B_{so}+B_\phi}{B}\right)\right] \quad (12)$$

with

$$F(z) = \ln(z) - \psi(1/2+z) \quad (13)$$

and

$$B_{\phi,so,e} = \hbar/4eL_{\phi,so,e}^2 \quad (14)$$

where ψ is the digamma function [35].

The magnetic-field dependent charge transport data shown in Fig. 5e and Fig. 6e were fitted to Eq. 9 and Eq. 12, respectively, using a Levenberg-Marquardt algorithm as implemented in the OriginLab software. In both cases, the curve measured at the lowest T, being most sensitive to the fit parameters, was fitted first, and the uncertainties were determined automatically by the software. The best-fit parameters of the curve were then used as the initial guesses for the fit to the next curve at larger T, and the procedure was repeated at all values of T. At high T, the experimental curves were sometimes too smooth for the fits to converge, due to mutual dependency between the free parameters. In this case, multiple fits were performed fixing one parameter at a time while leaving the other parameters free. The final values of the parameters were then obtained by averaging the results, and the uncertainties determined by their maximum differences.

DATA AVAILABILITY

The data that support the findings of this study are available at [https://data.hpc.imperial.ac.uk/] and from the authors upon reasonable request.

ACKNOWLEDGMENTS

F.T. acknowledges support from EPSRC grants EP/P02534X/2, EP/R511547/1, EP/T005106/1, and the Imperial College Collaboration Kick-Starter grant. E.P., F.G., D.D. and R.S.G. acknowledge support from the MIUR PRIN-2017 program (Grant No.2017Z8TS5B – "Tuning and understanding Quantum phases in 2D materials – Quantum2D"). L.A., K.A.P. and R.S. acknowledge support from the EU H2020 Graphene Flagship Core 3 Grant No. 881603. J.M.K. acknowledges support from EPSRC grant EP/P027628/1. V.N. acknowledges the support of the ERC CoG grant 3D2DPrint and of the SFI Centres AMBER and IForm. D.S., A.R., and A.Z. acknowledge support from the ERC CoG grant 3D2DPrint. A part of the electron microscopy characterization was carried out at the Advanced Microscopy Laboratory (AML) at the AMBER centre, CRANN Institute www.tcd.ie/crann/aml/, Trinity College Dublin, Ireland. AML is a Science Foundation Ireland (SFI)-supported imaging and analysis centre. We acknowledge Mr Federico La Barbera (Università di Catania) for the support in the morphological analysis of the ink-jet printed devices.

AUTHOR CONTRIBUTIONS

F.T. designed the study and directed the project. E.P., D.D. and R.S.G. designed and performed the electric transport measurements. A.A. synthesized the graphene and MoS_2 inks, fabricated the devices and performed the UV-Vis, AFM, Raman and XPS characterizations. E.P. and A.A. analysed the data. F.G. and L.A. contributed to the transport measurements and data analysis. T.C. contributed to the inks formulation and device fabrication. D.S. synthesised the MXene inks. A.R. and A.Z. perfomed the XPS characterisation and data analysis of the MXene inks. K.A.P. contributed to the device fabrication. F.T. and J.M.K. contributed to the interpretation of Raman, XPS, UV-Vis, and AFM data. R.S. designed the MoS_2 FET device and analysed the transport data.

E.P., A.A., D.D., R.S.G., V.N. and F.T. wrote the manuscript with input from all authors.

COMPETING INTERESTS

The authors declare no competing interests.

SUPPLEMENTARY INFORMATION

The supplementary material for this article is available at https://doi.org/10.1038/s41928-021-00684-9.

[1] Torrisi, F. & Carey, T. Graphene, related two-dimensional crystals and hybrid systems for printed and wearable electronics. *Nano Today* **23**, 73–96 (2018).

[2] Torrisi, F. & Coleman, J. N. Electrifying inks with 2D materials. *Nat. Nanotechnol.* **9**, 738–739 (2014).

[3] Carey, T. *et al.* Fully inkjet-printed two-dimensional material field-effect heterojunctions for wearable and textile electronics. *Nat. Commun.* **8**, 1202 (2017).

[4] Kelly, A. G. *et al.* All-printed thin-film transistors from networks of liquid-exfoliated nanosheets. *Science* **356**, 69–73 (2017).

[5] Li, J., Naiini, M. M., Vaziri, S., Lemme, M. C. & Östling, M. Inkjet printing of MoS_2. *Adv. Funct. Mater.* **24**, 6524–531 (2014).

[6] Karagiannidis, P. G. *et al.* Microfluidization of graphite and formulation of graphene-based conductive inks. *ACS Nano* **11**, 2742–2755 (2017).

[7] Ren, J. *et al.* Environmentally-friendly conductive cotton fabric as flexible strain sensor based on hot press reduced graphene oxide. *Carbon* **111**, 622–630 (2017).

[8] Qiang, S. *et al.* Wearable solid-state capacitors based on two-dimensional material all-textile heterostructures. *Nanoscale* **11**, 9912–9919 (2019).

[9] Parvez, K. *et al.* Exfoliation of graphite into graphene in aqueous solutions of inorganic salts. *J. Am. Chem. Soc.* **136**, 6083–6091 (2014).

[10] Lin, Z. *et al.* Solution-processable 2D semiconductors for high-performance large-area electronics. *Nature* **562**, 254–258 (2018).

[11] Paton, K. R. *et al.* Scalable production of large quantities of defect-free few-layer graphene by shear exfoliation in liquids. *Nat. Mater.* **13**, 624–630 (2014).

[12] Hernandez, Y. *et al.* High-yield production of graphene by liquid-phase exfoliation of graphite. *Nat. Nanotechnol.* **3**, 563–568 (2008).

[13] Hasan, T. *et al.* Solution-phase exfoliation of graphite for ultrafast photonics. *Phys. Stat. Sol. (B)* **247**, 2953–2957 (2010).

[14] Coleman, J. N. *et al.* Two-dimensional nanosheets produced by liquid exfoliation of layered materials. *Science* **331**, 568–571 (2011).

[15] Torrisi, F. *et al.* Inkjet-printed graphene electronics. *ACS Nano* **6**, 2992–3006 (2012).

[16] Kumar, D. K. *et al.* Scalable screen-printing manufacturing process for graphene oxide platinum free alternative counter electrodes in efficient dye sensitized solar cells. *FlatChem* **15**, 100105 (2019).

[17] Baker, J., Deganello, D., Gethin, D. T. & Watson, T. M. Flexographic printing of graphene nanoplatelet ink to replace platinum as counter electrode catalyst in flexible dye sensitised solar cell. *Mater. Res. Innov.* **18**, 86–90 (2014).

[18] Carey, T., Jones, C., Le Moal, F., Deganello, D. & Torrisi, F. Spray-coating thin films on three-dimensional surfaces for a semitransparent capacitive-touch device. *ACS Appl. Mater. Interfaces* **10**, 19948–19956 (2018).

[19] Sarycheva, A. *et al.* 2D titanium carbide (MXene) for wireless communication. *Sci. Adv.* **4**, eaau0920 (2018).

[20] Zhang, C. J. *et al.* Additive-free MXene inks and direct printing of micro-supercapacitors. *Nat. Commun.* **10**, 1795 (2019).

[21] Finn, D. J. *et al.* Inkjet deposition of liquid-exfoliated graphene and MoS_2 nanosheets for printed device applications. *J. Mater. Chem. C* **2**, 925–932 (2014).

[22] Micallef, F. G. *et al.* Transparent conductors for mid-infrared liquid crystal spatial light modulators. *Thin Solid Films* **660**, 411–420 (2018).

[23] Bianchi, V. *et al.* Terahertz saturable absorbers from liquid phase exfoliation of graphite. *Nat. Commun.* **8**, 15763 (2017).

[24] Wang, F. *et al.* Graphene passively Q-switched two-micron fiber lasers. In *2012 Conference on Lasers and Electro-Optics (CLEO)*, 1–2 (IEEE, 2012).

[25] Singh, M., Haverinen, H. M., Dhagat, P. & Jabbour, G. E. Inkjet printing – process and its applications. *Adv. Mater.* **22**, 673—685 (2010).

[26] Seo, J.-W. T. *et al.* Fully inkjet-printed, mechanically flexible MoS_2 nanosheet photodetectors. *ACS Appl. Mater. Interfaces* **11**, 5675–5681 (2019).

[27] Akinwande, D. Two-dimensional materials: printing functional atomic layers. *Nat. Nanotechnol.* **12**, 287–288 (2017).

[28] Ferrari, A. C. *et al.* Science and technology roadmap for graphene, related two-dimensional crystals, and hybrid systems. *Nanoscale* **7**, 4598–4810 (2015).

[29] Xue, J., Huang, S., Wang, J.-Y. & Xu, H. Q. Mott variable-range hopping transport in a MoS_2 nanoflake. *RSC Adv.* **9**, 17885–17890 (2019).

[30] Piatti, E. *et al.* Multi-valley superconductivity in ion-gated MoS_2 layers. *Nano Lett.* **18**, 4821–4830 (2018).

[31] Wu, C.-L. *et al.* Gate-induced metal-insulator transition in MoS_2 by solid superionic conductor LaF_3. *Nano Lett.* **18**, 2387–2392 (2018).

[32] Qiu, H. *et al.* Hopping transport through defect-induced localized states in molybdenum disulphide. *Nat. Commun.* **4**, 2642 (2013).

[33] Chen, J.-H., Jang, C., Xiao, S., Ishigami, M. & Fuhrer, M. S. Intrinsic and extrinsic performance limits of graphene devices on SiO_2. *Nat. Nanotechnol.* **3**, 206–209 (2008).

[34] Park, C.-H. *et al.* Electron–phonon interactions and the intrinsic electrical resistivity of graphene. *Nano Lett.* **14**, 1113–1119 (2014).

[35] Gonnelli, R. S. *et al.* Weak localization in electric-double-layer gated few-layer graphene. *2D Mater.* **4**, 035006 (2017).

[36] Miranda, A., Halim, J., Barsoum, M. W. & Lorke, A. Electronic properties of freestanding $Ti_3C_2T_x$ MXene monolayers. *Appl. Phys. Lett.* **108**, 033102 (2016).

[37] Lipatov, A. *et al.* Effect of synthesis on quality, electronic properties and environmental stability of individual monolayer Ti_3C_2 MXene flakes. *Adv. Electron. Mater.* **2**, 1600255 (2016).

[38] Sangwan, V. K. & Hersam, M. C. Electronic transport in two-dimensional materials. *Annu. Rev. Phys. Chem.* **69**, 299–325 (2018).

[39] Kravets, V. G. *et al.* Spectroscopic ellipsometry of graphene and an exciton-shifted van Hove peak in absorption. *Phys. Rev. B* **81**, 155413 (2010).

[40] Eda, G. *et al.* Photoluminescence from chemically exfoliated MoS_2. *Nano Lett.* **11**, 5111–5116 (2011).

[41] Wilcoxon, J. P., Newcomer, P. P. & Samara, G. A. Synthesis and optical properties of MoS_2 and isomorphous nanoclusters in the quantum confinement regime. *J. Appl. Phys.* **81**, 7934–7944 (1997).

[42] Hu, M. *et al.* Surface functional groups and interlayer water determine the electrochemical capacitance of $Ti_3C_2T_x$ MXene. *ACS Nano* **12**, 3578–3586 (2018).

[43] Hope, M. A. *et al.* NMR reveals the surface functionalisation of Ti_3C_2 MXene. *Phys. Chem. Chem. Phys.* **18**, 5099–5102 (2016).

[44] Satheeshkumar, E. *et al.* One-step solution processing of Ag, Au and Pd@ MXene hybrids for SERS. *Sci. Rep.* **6**, 32049 (2016).

[45] Dillon, A. D. *et al.* Highly conductive optical quality solution-processed films of 2D titanium carbide. *Adv. Funct. Mater.* **26**, 4162–4168 (2016).

[46] El-Demellawi, J. K., Lopatin, S., Yin, J., Mohammed, O. F. & Alshareef, H. N. Tunable multipolar surface plasmons in 2D $Ti_3C_2T_x$ MXene flakes. *ACS Nano* **12**, 8485–8493 (2018).

[47] Hantanasirisakul, K. & Gogotsi, Y. Electronic and optical properties of 2D transition metal carbides and nitrides (MXenes). *Adv. Mater.* **30**, 1804779 (2018).

[48] Liu, G. *et al.* Surface modified Ti_3C_2 MXene nanosheets for tumor targeting photothermal/photodynamic/chemo synergistic therapy. *ACS Appl. Mater. Interfaces* **9**, 40077–40086 (2017).

[49] Hoath, S. D. *Fundamentals of Inkjet Printing: The Science of Inkjet and Droplets* (John Wiley & Sons, 2016).

[50] Kang, R. *et al.* Enhanced thermal conductivity of epoxy composites filled with 2D transition metal carbides (MXenes) with ultralow loading. *Sci. Rep.* **9**, 9135 (2019).

[51] Schier, V., Michel, H.-J. & Halbritter, J. ARXPS-analysis of sputtered TiC, SiC and $Ti_{0.5}Si_{0.5}C$ layers. *Fresenius J. Anal. Chem.* **346**, 227–232 (1993).

[52] García-Romeral, N., Keyhanian, M., Morales-García, Á. & Illas, F. Relating X-ray photoelectron spectroscopy data to chemical bonding in MXenes. *Nanoscale Adv.* **3**, 2793–2801 (2021).

[53] Natu, V. *et al.* A critical analysis of the x-ray photoelectron spectra of $Ti_3C_2T_z$ MXenes. *Matter* **4**, 1224–1251 (2021).

[54] Myhra, S., Crossley, J. A. A. & Barsoum, M. W. Crystal-chemistry of the Ti_3AlC_2 and Ti_4AlN_3 layered carbide/nitride phases—characterization by XPS. *J. Phys. Chem. Solids* **62**, 811–817 (2001).

[55] Ferrari, A. C. & Basko, D. M. Raman spectroscopy as a versatile tool for studying the properties of graphene. *Nat. Nanotechnol.* **8**, 235–246 (2013).

[56] Secor, E. B., Ahn, B. Y., Gao, T. Z., Lewis, J. A. & Hersam, M. C. Rapid and versatile photonic annealing of graphene inks for flexible printed electronics. *Adv. Mater.* **27**, 6683–6688 (2015).

[57] Parkin, W. M. *et al.* Raman shifts in electron-irradiated monolayer MoS_2. *ACS Nano* **10**, 4134–4142 (2016).

[58] Acerce, M., Voiry, D. & Chhowalla, M. Metallic 1T phase MoS_2 nanosheets as supercapacitor electrode materials. *Nat. Nanotechnol.* **10**, 313–318 (2015).

[59] De, S., King, P. J., Lyons, P. E., Khan, U. & Coleman, J. N. Size effects and the problem with percolation in nanostructured transparent conductors. *ACS Nano* **4**, 7064–7072 (2010).

[60] Mott, N. F. & Davis, E. A. *Electronic Processes in Non-crystalline Materials* (Oxford University Press, Oxford, 1979).

[61] Mott, N. F. *Metal-Insulator Transition* (Taylor & Francis, London, 1990).

[62] Beloborodov, I. S., Lopatin, A. V., Vinokur, V. M. & Efetov, K. B. Granular electronic systems. *Rev. Mod. Phys.* **79**, 469 (2007).

[63] Halim, J. *et al.* Transparent conductive two-dimensional titanium carbide epitaxial thin films. *Chem. Mater.* **26**, 2374–2381 (2014).

[64] Wang, H., Wu, Y., Cong, C., Shang, J. & Yu, T. Hysteresis of electronic transport in graphene transistors. *ACS Nano* **4**, 7221–7228 (2010).

[65] Wang, F. *et al.* Inter-flake quantum transport of electrons and holes in inkjet-printed graphene devices. *Adv. Funct. Mater.* **31**, 2007478 (2021).

[66] Carey, T. *et al.* Inkjet printed circuits with 2D semiconductor inks for high-performance electronics. *Adv. Electron. Mater.* **7**, 2100112 (2021).

[67] Li, G. *et al.* Equilibrium and non-equilibrium free carrier dynamics in 2D $Ti_3C_2T_x$ MXenes: THz spectroscopy study. *2D Mater.* **5**, 035043 (2018).

[68] Emelianova, E. V., Van der Auweraer, M., Adriaenssens, G. J. & Stesmans, A. Carrier mobility in two-dimensional disordered hopping systems. *Org. Electron.* **9**, 29–135 (2008).

[69] Ippolito, S. *et al.* Covalently interconnected transition metal dichalcogenide networks via defect engineering for high-performance electronic devices. *Nat. Nanotechnol.* **16**, 592–598 (2021).

[70] Halim, J. *et al.* Variable range hopping and thermally activated transport in molybdenum-based MXenes. *Phys. Rev. B* **98**, 104202 (2018).

[71] Hart, J. L. *et al.* Control of MXenes' electronic properties through termination and intercalation. *Nat. Commun.* **10**, 522 (2019).

[72] Kovtun, A. *et al.* Multiscale charge transport in van der Waals thin films: Reduced graphene oxide as a case study. *ACS Nano* **15**, 2654–2667 (2021).

[73] Kim, J. S. *et al.* Electrical transport properties of polymorphic MoS_2. *ACS Nano* **10**, 7500–7506 (2016).

[74] Grimaldi, C., Ryser, P. & Strässler, S. Gauge factor of thick-film resistors: Outcomes of the variable-range-hopping model. *J. Appl. Phys.* **88**, 4164–4169 (2000).

[75] Rodríguez, M., Bonalde, I. & Medina, E. Consistent hopping criterion in the Efros-Shklovskii regime. *Phys.*

Rev. B **75**, 235505 (2007).

[76] Liu, C.-I. *et al.* Variable range hopping and nonlinear transport in monolayer epitaxial graphene grown on SiC. *Semicond. Sci. Technol.* **31**, 105008 (2016).

[77] Bostwick, A. *et al.* Quasiparticle transformation during a metal-insulator transition in graphene. *Phys. Rev. Lett.* **103**, 056404 (2009).

[78] Elias, D. C. *et al.* Control of graphene's properties by reversible hydrogenation: evidence for graphane. *Science* **323**, 610–613 (2009).

[79] Adkins, C. J., Benjamin, J. D., Thomas, J. M. D., Gardner, J. W. & McGeown, A. J. Potential disorder in granular metal systems: the field effect in discontinuous metal films. *J. Phys. C: Solid State Phys.* **17**, 4633 (1984).

[80] Su, T.-I., Wang, C.-R., Lin, S.-T. & Rosenbaum, R. Magnetoresistance of $Al_{70}Pd_{22.5}Re_{7.5}$ quasicrystals in the variable-range hopping regime. *Phys. Rev. B* **66**, 054438 (2002).

[81] Ando, T., Fowler, A. B. & Stern, F. Electronic properties of two-dimensional systems. *Rev. Mod. Phys.* **54**, 437 (1982).

[82] Beenakker, C. W. J. & van Houten, H. Quantum transport in semiconductor nanostructures. *Solid State Phys.* **44**, 1–228 (1991).

[83] Barua, S., Hatnean, M. C., Lees, M. & Balakrishnan, G. Signatures of the Kondo effect in VSe_2. *Sci. Rep.* **7**, 10964 (2017).

[84] Pippard, A. B. *Magnetoresistance in Metals* (Cambridge University Press, Cambridge, 1989).

[85] Hikami, S., Larkin, A. I. & Nagaoka, Y. Spin-orbit interaction and magnetoresistance in the two dimensional random system. *Prog. Theor. Phys.* **63**, 707–710 (1980).

[86] Edmonds, M. T. *et al.* Spin–orbit interaction in a two-dimensional hole gas at the surface of hydrogenated diamond. *Nano Lett.* **15**, 16–20 (2015).

[87] Piatti, E. *et al.* Ambipolar suppression of superconductivity by ionic gating in optimally doped $BaFe_2(As,P)_2$ ultrathin films. *Phys. Rev. Materials* **3**, 044801 (2019).

[88] Ooi, N., Rairkar, A. & Adams, J. B. Density functional study of graphite bulk and surface properties. *Carbon* **44**, 231–242 (2006).